RESEARCH ARTICLE

Multimodal Spatial Profiling Reveals Immune Suppression and Microenvironment Remodeling in Fallopian Tube Precursors to High-Grade Serous Ovarian Carcinoma

Tanjina Kader[1,2], Jia-Ren Lin[1,2], Clemens B. Hug[1], Shannon Coy[1,2,3], Yu-An Chen[1,2], Ino de Bruijn[4], Natalie Shih[5], Euihye Jung[5], Roxanne J. Pelletier[1], Mariana Lopez Leon[1], Gabriel Mingo[5], Dalia K. Omran[5], Jong Suk Lee[1,2], Clarence Yapp[1,2], Baby A. Satravada[4], Ritika Kundra[4], Yilin Xu[1,2,3], Sabrina Chan[1,2], Juliann B. Tefft[1], Jeremy L. Muhlich[1], Sarah H. Kim[5], Stefan M. Gysler[5], Judith Agudo[6], James R. Heath[7,8], Nikolaus Schultz[4], Charles W. Drescher[9], Peter K. Sorger[1,2,10], Ronny Drapkin[5,11], and Sandro Santagata[1,2,3,10]

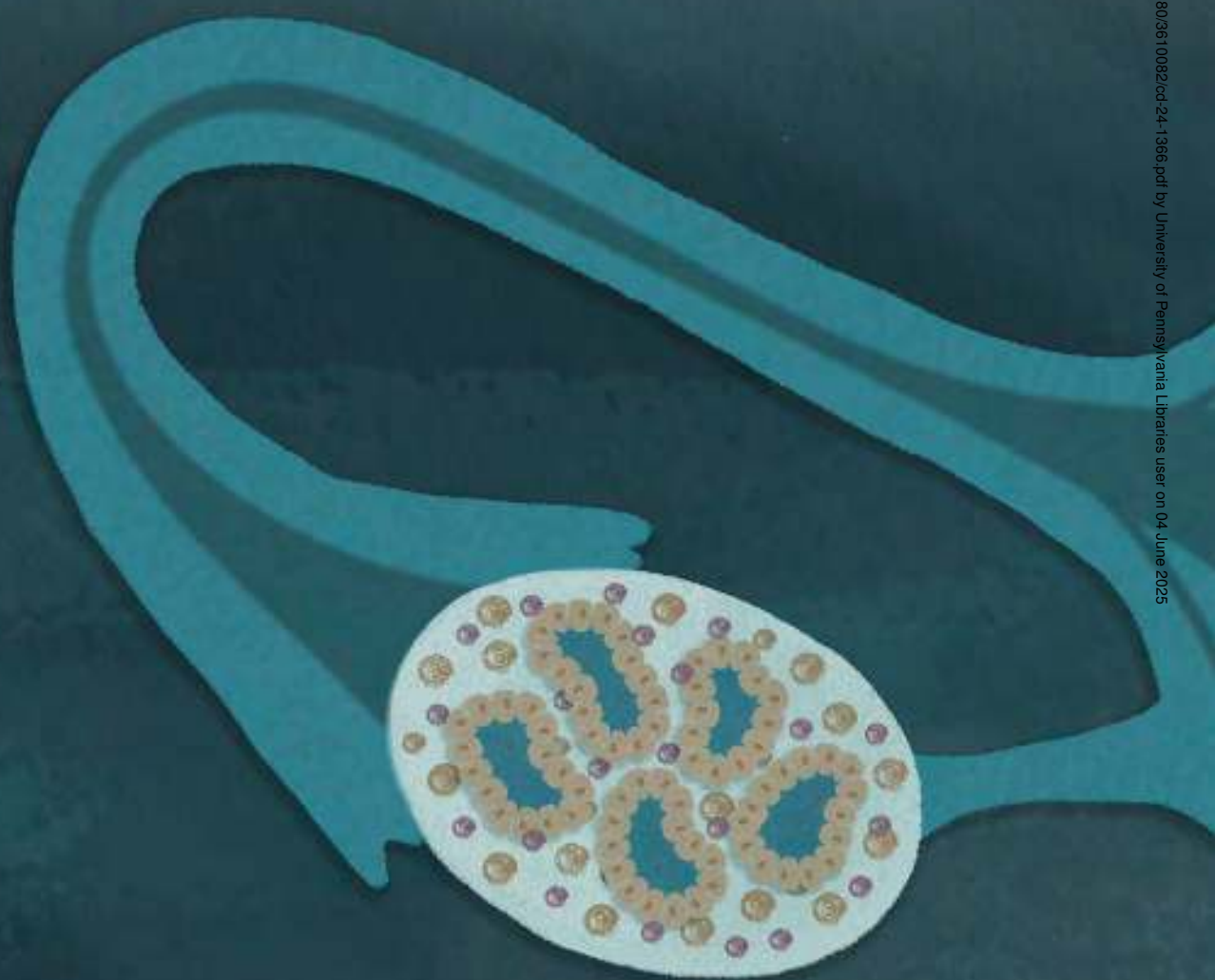

ABSTRACT High-grade serous ovarian cancer (HGSOC) originates from fallopian tube (FT) precursors. However, the molecular changes that occur as precancerous lesions progress to HGSOC are not well understood. To address this, we integrated high-plex imaging and spatial transcriptomics to analyze human tissue samples at different stages of HGSOC development, including p53 signatures, serous tubal intraepithelial carcinomas (STIC), and invasive HGSOC. Our findings reveal immune modulating mechanisms within precursor epithelium, characterized by chromosomal instability, persistent IFN signaling, and dysregulated innate and adaptive immunity. FT precursors display elevated expression of MHC class I, including HLA-E, and IFN-stimulated genes, typically linked to later-stage tumorigenesis. These molecular alterations coincide with progressive shifts in the tumor microenvironment, transitioning from immune surveillance in early STICs to immune suppression in advanced STICs and cancer. These insights identify potential biomarkers and therapeutic targets for HGSOC interception and clarify the molecular transitions from precancer to cancer.

SIGNIFICANCE: This study maps the immune response in FT precursors of HGSOC, highlighting localized IFN signaling, chromosomal instability, and competing immune surveillance and suppression along the progression axis. It provides an explorable public spatial profiling atlas for investigating precancer mechanisms, biomarkers, and early detection and interception strategies.

See related commentary by Recouvreux and Orsulic, p. 1093

INTRODUCTION

High-grade serous ovarian carcinoma (HGSOC) is a highly aggressive gynecologic cancer, causing more than 200,000 deaths worldwide each year (1). The absence of early-stage symptoms often results in diagnosis at advanced stages (American Joint Committee on Cancer stages III and IV) when the cancer has already spread. The 5-year overall survival rate for patients with advanced disease is less than 30% and has remained unchanged for decades (2). Standard treatment includes surgery to reduce tumor burden, followed by chemotherapy, but chemoresistance is common, with more than 80% of stage III or IV patients experiencing relapse after initial treatment. This underscores the need for early detection and interception strategies to identify the disease at its earliest stages, reduce recurrence, and improve outcomes (3). Women with *BRCA* gene mutations are at particularly high risk for developing HGSOC, leading some women to choose preventive surgery, such as bilateral salpingectomy-oophorectomy (BSO) to reduce their risk (3).

Over the past 2 decades, studies have shown that HGSOC originates at the distal, fimbriated end of the fallopian tube (FT; refs. 4–6). Histopathologic evaluation and next-generation sequencing have recognized two types of precursor lesions for HGSOC: the "p53 signature" and serous tubal intraepithelial carcinomas (STIC). p53 signatures are benign-appearing stretches of secretory cells with *TP53* mutations; the cells are nonproliferative and commonly located at the fimbriated end of the FT, regardless of genetic risk. The origin of these p53 signatures is linked to the 'incessant ovulation hypothesis,' which proposes that continuous ovulation leads to repeated injury to cells near ruptured follicles, including those at the fimbriated end of the FT (7). The repeated injury leads to genetic and epigenetic alterations, transforming p53 signatures into STICs and eventually into invasive cancer (8). Incidental STICs (STIC.I) discovered during risk-reduction surgeries have been associated with the subsequent development of peritoneal carcinomatosis (9), suggesting that STIC cells may shed from the fimbria before invasion occurs [a precursor escape model (10)]. However, the progression of these precursors to invasive cancer is complex, and the steps are not yet fully understood.

Genomic studies have demonstrated a clonal relationship between p53 signatures, STICs, and concurrent HGSOCs, with each sharing identical *TP53* mutations (11–13). Nearly half of HGSOCs exhibit defects in homologous recombination, resulting in genomic instability due to somatic mutations in

[1]Laboratory of Systems Pharmacology, Harvard Medical School, Boston, Massachusetts. [2]Ludwig Center at Harvard, Boston, Massachusetts. [3]Department of Pathology, Brigham and Women's Hospital, Harvard Medical School, Boston, Massachusetts. [4]Memorial Sloan Kettering Cancer Center, New York, New York. [5]Department of Obstetrics and Gynecology, Penn Ovarian Cancer Research Center, University of Pennsylvania Perelman School of Medicine, Philadelphia, Pennsylvania. [6]Department of Cancer Immunology and Virology, Dana-Farber Cancer Institute, Boston, Massachusetts. [7]Institute of Systems Biology, Seattle, Washington. [8]Department of Bioengineering, University of Washington, Seattle, Washington. [9]Swedish Cancer Institute Gynecologic Oncology and Pelvic Surgery, Seattle, Washington. [10]Department of Systems Biology, Harvard Medical School, Boston, Massachusetts. [11]Basser Center for BRCA, Abramson Cancer Center, University of Pennsylvania School of Medicine, Philadelphia, Pennsylvania.

T. Kader, J.-R. Lin, and C.B. Hug contributed equally to this article.

R. Drapkin and S. Santagata contributed equally to this article.

Corresponding Author: Sandro Santagata, Laboratory of Systems Pharmacology, 200 Longwood Avenue, Armenise Building Room 109, Boston, MA 02115. E-mail: ssantagata@bwh.harvard.edu

Cancer Discov 2025;15:1180–202

doi: 10.1158/2159-8290.CD-24-1366

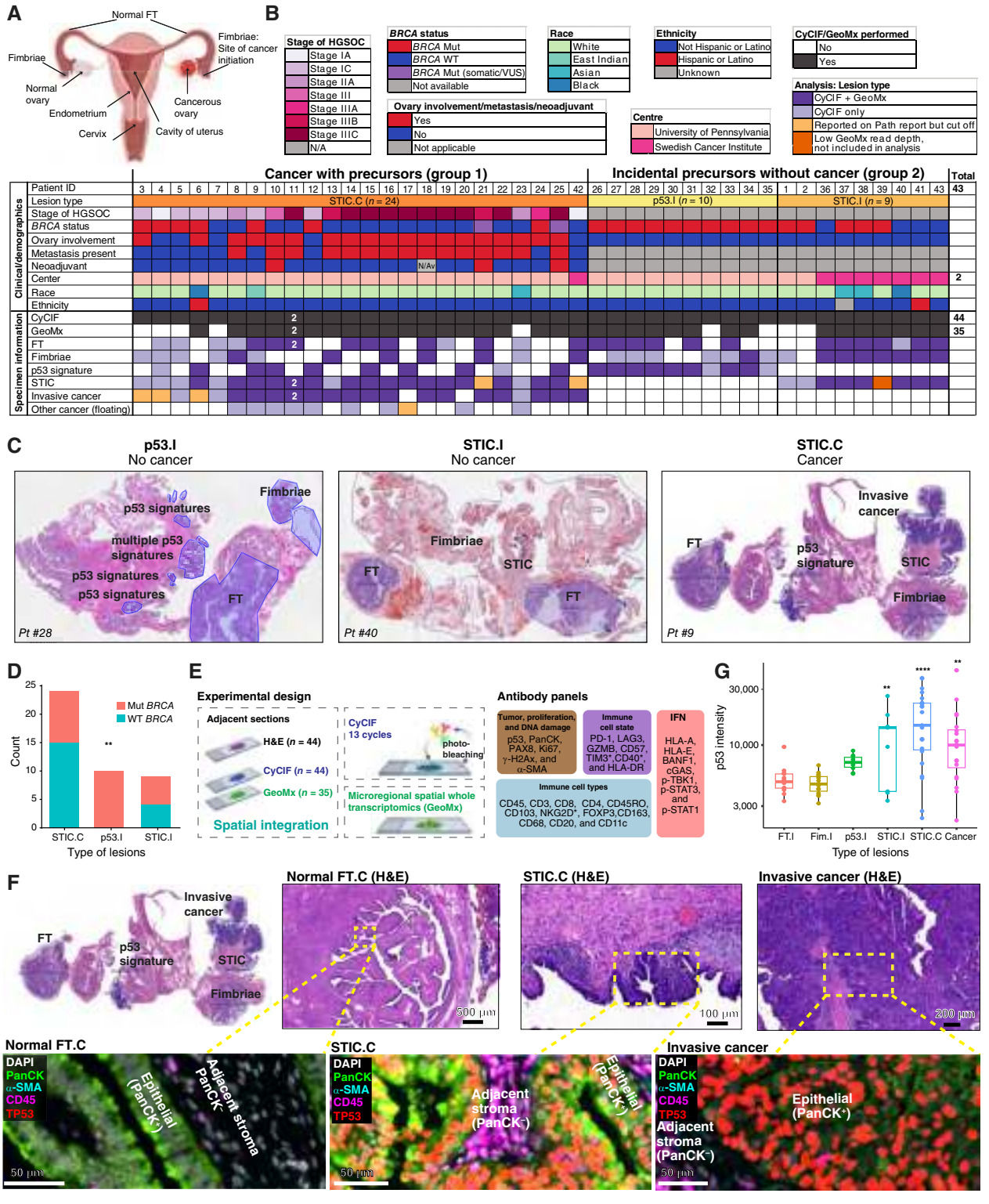

Figure 1. Overview of the patient cohort and experimental design. **A,** Schematic of the female reproductive tract highlighting the FT, its distal fimbriated end, and the ovary. It is now generally accepted that HGSOCs arise from secretory cells located at the distal fimbriated end of the FT. **B,** Summary of clinical annotations for the 43-patient cohort. A total of 44 specimens were analyzed by tissue CyCIF and 35 specimens by spatial transcriptomics (GeoMx; NanoString). The annotations include lesion types (histology), HGSOC stage, *BRCA* mutation status, ovarian involvement, metastasis, neoadjuvant chemotherapy, patient demographics, and whether lesions were lost in subsequent H&E sections (N/Av). Additional details are provided in Supplementary Table S1. **C,** Representative H&E images showing labeled examples from each subgroup: p53.I, STIC.I, and STIC.C. **D,** A stacked bar plot comparing the number of *BRCA* mutant (Mut) and WT cases between incidental and cancer-associated precancer lesions; **, $P < 0.01$, Fisher's exact test. **E,** Experimental design illustrating the integration of multiplex tissue imaging (CyCIF) and spatial transcriptomics (GeoMx), (*continued on following page*)

the *BRCA1/2* genes, epigenetic silencing of *BRCA1/2* promoters, or mutations in other DNA repair factors (3). HGSOC also commonly displays chromosomal instability (CIN), including breakage-fusion-bridge cycles that lead to the amplification of key oncogenes such as *CCNE1* (14). DNA methylation analyses further support the FT as the origin of HGSOC, as the methylation profile of HGSOC more closely resembles that of FT epithelium than ovarian surface epithelium (15, 16). In addition, HGSOC-specific hypermethylation is present exclusively in the FT epithelium of women with STIC lesions (17). Early events in STICs include similar global patterns of copy-number alterations, such as *CCNE1* amplification and higher ploidy (11–13, 18–21).

Despite progress in understanding these genetic features, the role of the immune microenvironment in HGSOC development and progression remains underexplored. Among the four subtypes of HGSOC, the immunoreactive subtype, characterized by $CD8^+$ cytotoxic T lymphocyte (CTL) infiltration, is associated with a better prognosis (22, 23). By contrast, subtypes such as the C5/PRO subtype often exhibit immune deserts or CTL exclusion, which are linked to poorer outcomes (24). Single-cell RNA sequencing of advanced HGSOC has identified several cancer-related pathways, including JAK–signal transducer and activator of transcription (STAT) signaling, the IFN response, inflammatory pathways, and TGF-β signaling, all of which correlate with T-cell infiltration levels (25). The female reproductive tract (including the FTs) has a highly active immune system, rich in NK and T cells, which are likely involved in maintaining immune tolerance during pregnancy and monitoring microbial infections (26, 27). Thus, gaining a better understanding of how the immune microenvironment changes during HGSOC progression could provide key insights into improving disease diagnosis and management.

In this study, we used a multi-omics approach to map the tumor-immune ecosystems during the development and progression of HGSOC. We leveraged several high-plex spatial analysis methods, such as cyclic immunofluorescence [CyCIF (28)], 3D CyCIF (Yapp and colleagues, bioRxiv 2024), and spatial transcriptomics (whole transcriptome analysis, WTA; ref. 29) of human archival tissue specimens to map the spatial distributions, interactions, and molecular programs of different cell types. These data reveal key changes that occur in the tumor microenvironment (TME) as precancerous STIC lesions progress to invasive HGSOC. We uncover temporal changes in molecular pathways, including activation of IFN signaling, micronuclei (MN) formation and rupture, and cyclic GMP-AMP synthase (cGAS)-stimulator of IFN genes (STING) signaling. CyCIF imaging reveals dynamic shifts in immune cell populations and interactions over the progression axis. Early lesions are defined by active immune surveillance characterized by the presence of type 1 conventional dendritic cells (cDC1), NK cells, and tissue-resident memory (T_{RM}) $CD8^+$ T cells. However, in advanced precursor lesions, we observe a significant decline in these immune cells, along with molecular evidence of immune dysfunction and immune editing. By combining spatial transcriptomics and high-plex tissue imaging, this study highlights the dynamic interplay between immune activation, suppression, and molecular reprogramming during HGSOC progression. We have made our data publicly available and explorable through cBioPortal, providing a widely accessible resource for identifying therapeutic targets and informing early detection strategies.

RESULTS

Specimen Cohort

To investigate the molecular and spatial changes occurring in the FT during the early development of HGSOC, we analyzed 44 FT specimens with precursor lesions collected from 43 individuals obtained from a multicenter collaboration (Fig. 1A–C). The 44 specimens were collected from patients with various genotypes and disease presentations, which we categorized into two main groups based on the presence or absence of cancer. Specimens in group 1 (n = 24) contained invasive cancer and co-occurring STIC (denoted as STIC.C). This included specimens from individuals with and without *BRCA* mutations [wild-type (WT) *BRCA* 15/24; germline (g) *BRCA* $n = 7/9$; g*BRCA2* $n = 6/7$; somatic 2/9; Fig. 1B–D)]. Specimens in group 2 ($n = 19$) lacked invasive cancer but contained precursor lesions that were identified during risk-reducing BSO or opportunistic salpingectomy. Group 2 included patients with and without *BRCA* mutations, and specimens contained incidental p53 signatures (denoted as p53.I, $n = 10$; g*BRCA*1 5/10; g*BRCA*2 5/10) and STIC.I lesions ($n = 9$; g*BRCA* 5/9; g*BRCA*2 1/5; WT *BRCA* 4/9; Fig. 1B–D). STIC.I likely represents early time points in clonal evolution, whereas STIC.C represents later points in the development and progression of STIC lesions (12, 30, 31). Of the 44 specimens, all but nine had matched FT and/or fimbriae (Fim) within the same tissue section (Fig. 1C).

Among the 24 patients with invasive cancer, eight had stage I disease (6/8 with g*BRCA* mutations). Five of these stage I patients had tumors restricted to the FT, with no involvement of the ovary or spread through the abdomen (peritoneal metastasis; Supplementary Fig. S1A and S1B). The remaining 16 patients had stage II to III disease (13/16 *BRCA* WT). Only three patients with cancer received neoadjuvant chemotherapy, whereas the rest had surgery without prior chemotherapy

Figure 1. ***(Continued)*** from adjacent 5-μm sections, guided by histology. GeoMx ROIs were registered with CyCIF images using X/Y coordinates (see Supplementary Fig. S2 and "Methods"). The CyCIF panel included 31 antibodies, some of which (indicated with asterisks) were only used on a subset of the specimens ($n = 26/44$). High-resolution 3D CyCIF was performed for one STIC.C case (patient ID 9, case RD-23-002), shown in **F**. **F,** Example of STIC with concurrent HGSOC (case RD-23-002, patient ID 9, *BRCA2* mutant, stage IC HGSOC). H&E images (top row) show the different histologies present: normal FT (FT.C), STIC.C, and invasive cancer. Selected CyCIF markers (bottom row) illustrate mutant p53 expression in epithelial cells ($PanCK^+$) within the lesional regions. The adjacent stroma lacks PanCK expression ($PanCK^-$). **G,** Box plot comparing p53 intensity (in relative fluorescence units) measured by CyCIF in the epithelial compartment across various disease stages. The *Y*-axis is on a $\log_{10}$ scale. Sample sizes were as follows: FT.I ($n = 13$), Fim.I ($n = 15$), p53.I ($n = 10$), STIC.I ($n = 9$), STIC.C ($n = 23$), and cancer ($n = 20$). The median is indicated by a horizontal solid line, and whiskers extend to 1.5× the IQR. Outliers are shown as individual points. Black asterisks indicate significant differences from FT.I determined by LMMs with patient ID as a random effect (**, $P < 0.01$; ****, $P < 0.0001$) using the lme4 R package (version 4.3.3). PanCK, pan-cytokeratin, DAPI, 4′,6-diamidino-2-phenylindole. (**A** and **E,** Created with BioRender.com.)

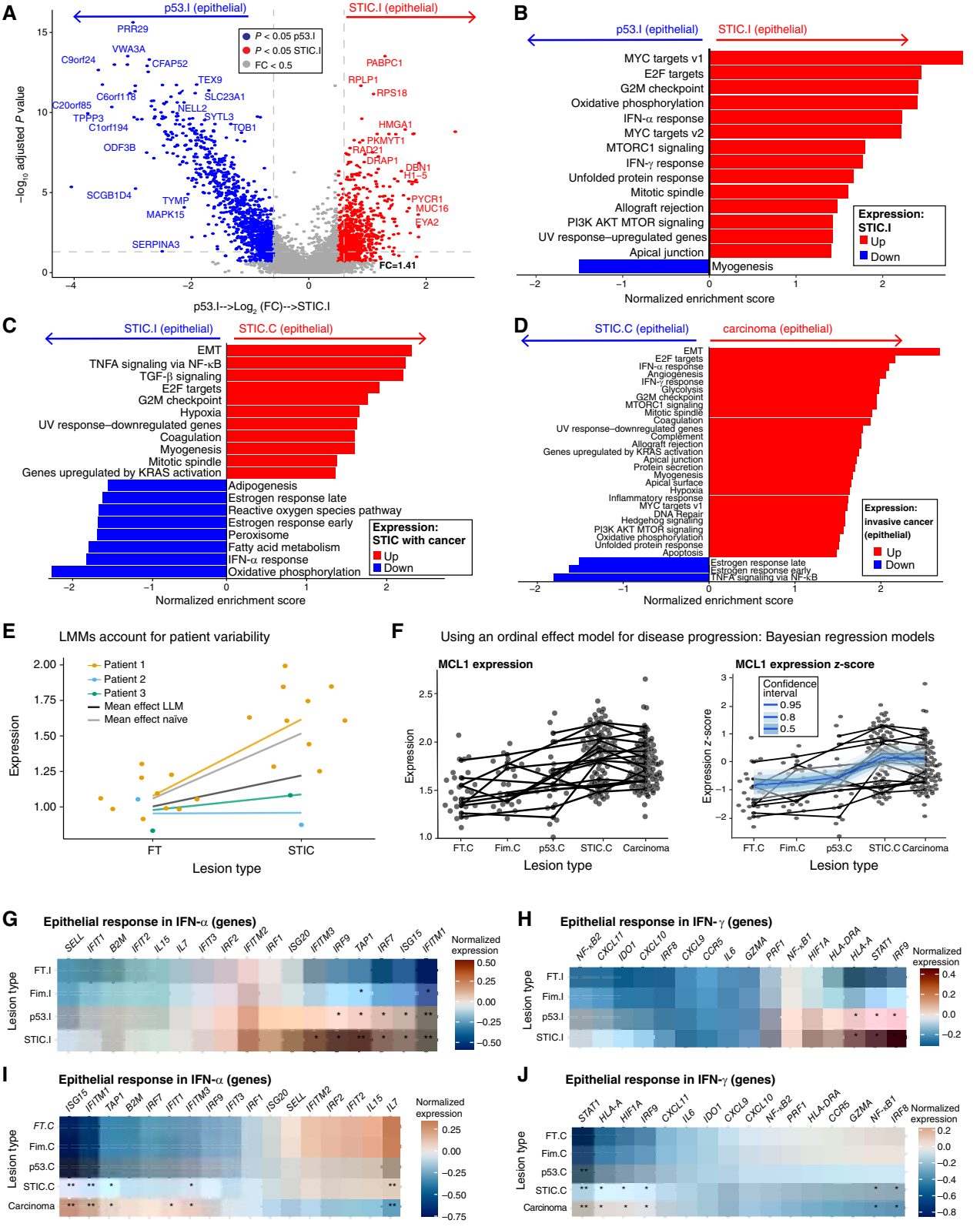

Figure 2. Molecular transitions during HGSOC development using spatial transcriptomics. **A,** We examined differential gene expression in epithelial compartments between p53.I ($n = 39$ ROIs) and STIC.I ($n = 27$ ROIs) using a LMM. The model included lesion type as a fixed effect and scan_ID (representing patient/slide ID) as a random intercept. Benjamini–Hochberg correction was applied using GeoMx DSP software (NanoString, version 3.1.0.221). The model formula was as follows: gene expression ~ lesion_type + (1|scan_ID). Only a subset of differentially expressed genes is shown. **B–D,** GSEA was performed on differentially expressed genes in the epithelial compartment using GeoMx DSP software. Using MsigDB (*continued on following page*)

(treatment-naïve; Fig. 1B). Patients with invasive cancer and STIC.C were much older (median age of 65.5 years, range, 46–85; Supplementary Fig. S1C) than individuals with incidental precursor lesions (p53.I or STIC.I; median age of 47 years, range, 34–72). The younger age of individuals with incidental lesions reflects earlier timing of BSO in women with known *BRCA* mutations. Overall, this cohort represents the entire spectrum of HGSOC development, enabling the characterization of disease progression (Fig. 1B; Supplementary Table S1).

Precursor and Cancer Analysis with CyCIF and Spatial Transcriptomics

We analyzed tissue sections from all 44 specimens using hematoxylin and eosin (H&E) staining and CyCIF (28), which was performed using a panel of 31 antibodies and quantified to reveal protein expression at the single-cell level (Fig. 1E; refs. 28, 32). Multiple pathologists reviewed the H&E and CyCIF images to identify and classify precursor lesions and cancer (Fig. 1B and F). Compared with samples with STIC.I lesions, STIC.C displayed a greater number of discrete STIC lesions (median: 5 STIC.C vs. 2 STIC.I; Supplementary Fig. S1D) and larger lesion size, indicated by a higher number of epithelial cells per lesion (Supplementary Fig. S1E). As expected, CyCIF analysis revealed elevated p53 protein levels in p53.I, STIC.I, STIC.C, and cancer compared with normal epithelium (FT.I; Fig. 1F and G), consistent with the role of mutant p53 in HGSOC development (33, 34). In addition, we observed a progressive increase in proliferation (Ki67+ cells) and DNA damage (γH2Ax^{+} cells) with disease progression (Supplementary Fig. S1F–S1I). Interestingly, STIC.I lesions exhibited significant variability in both proliferation and DNA damage, suggesting the potential for further subtyping of these incidental lesions based on their molecular characteristics (Supplementary Fig. S1F and S1G).

Spatial transcriptomic analysis (GeoMx) was performed on an adjacent tissue section to measure gene expression across the entire transcriptome, within specified tissue regions (Fig. 1E; Supplementary Fig. S2A). The H&E and CyCIF images were used to select regions of interest (ROI) for GeoMx analysis, which included normal epithelium (FT and/or Fim), precursor epithelium, regions of the tumor, and stroma adjacent to most of the ROI (Supplementary Fig. S2A and S2B; see "Methods"; ROI annotation in Supplementary Table S2). Of the 44 specimens, 35 had sufficient material for GeoMx analysis (see "Methods"). Principal component analysis of this spatial transcriptomic data revealed that epithelial and stroma ROIs segregated along the first principal component (PC1), whereas the second principal component (PC2) distinguished between incidental precursors and cancer ROIs, reflecting their biological differences (Supplementary Figs. S2C, S3A, and S3B).

Molecular Transitions during HGSOC Development

HGSOC development is a multi-stage process driven by genetic and molecular alterations influenced by selective pressures (3, 31). To understand the transitions between the stages of HGSOC development, we analyzed the differential gene expression patterns within the epithelium across various stages of the disease using spatial transcriptomics data (Fig. 2A–J). Gene set enrichment analysis (GSEA; refs. 35, 36) revealed prominent activation of the IFN pathway (both IFNα and IFNγ) and cell-cycle regulator pathways in the epithelium during early HGSOC development. This activation was evident comparing normal epithelium of incidental FT (FT.I) and incidental Fim (Fim.I) to p53.I (Supplementary Fig. S4A) and p53.I to STIC.I (Fig. 2A and B).

As the disease progressed, STIC.C lesions (regardless of *BRCA* status) displayed further enrichment of the IFN response as well as genes associated with TGF-β signaling, epithelial-to-mesenchymal transition (EMT), hypoxia, and TNF-α signaling via the NFκB pathway (Fig. 2C; Supplementary Fig. S4B). These pathways were further upregulated in established cancer (Fig. 2D), promoting invasion, motility, stress adaptation, and inflammation. Interpreting the presence of EMT in precursor and cancer lesions can be challenging particularly considering that fibroblasts constitute a major component of most cancers, and these cells also express mesenchymal and EMT-related markers (37, 38).

Figure 2. ***(Continued)*** Cancer Hallmark gene sets, we identified pathways associated with disease progression in three comparisons: (**B**) p53.I ($n = 39$ ROIs) vs. STIC.I ($n = 27$ ROIs), showing enrichment of IFN and proliferative pathways; (**C**) STIC.I ($n = 27$ ROIs) vs. STIC.C ($n = 96$ ROIs), highlighting EMT, TGF-β, and hypoxia pathways; and (**D**) STIC.C ($n = 96$ ROIs) vs. invasive carcinoma ($n = 105$ ROIs), associated with angiogenesis and Hedgehog signaling. Pathway are ranked by adjusted P values <0.05. **E–J,** Because LMMs and GSEA are limited to pairwise comparisons, we applied Bayesian regression modeling to analyze the full progression from normal FT to cancer. Bayesian models are advantageous because they account for repeated sampling from the same patient. **E,** A synthetic example illustrates how repeated samples from a single patient (patient 1) can skew the mean effect if patient variability is not considered. LMMs address this by incorporating patient-level random effects. **F,** We further advanced the approach with Bayesian ordinal regression to model gene expression across multiple disease stages, using *MCL1* as an example. In contrast to LMMs in GeoMx DSP software – which only support pairwise comparisons with a single random effect – Bayesian ordinal regression can handle multiple disease stages simultaneously. We used the "brms" R package and imposed a monotonic constraint (mo) to represent orderly lesion progression (44). GeoMx expression counts were Q3-normalized for sequencing depth (see "Methods") and then log-transformed to stabilize variance. To standardize across genes (thus accounting for gene expression variability), we z-transformed these values to a mean of zero and variance of one. For each gene, we fitted the model: gene_expression ~ mo(stage) + [1 + mo(stage)|patient_id]. Here, the monotonic constraint ensures ordered progression (44), and patient-specific effects are modeled through random intercepts and stage coefficients. For gene set analyses, additional random effects were included: gene_expression ~ mo(stage) + [1 + mo(stage)|patient_id * gene] (see "Methods" for further details). **G–J,** To investigate IFN pathway changes from normal FT to STIC (incidental or cancer-associated) and then to carcinoma, we used the Bayesian ordinal regression model to identify IFN hallmark genes. This approach compares relative gene expression changes in both the epithelial and stromal compartments across disease stages relative to their matched FT. The heatmaps illustrate normalized gene expression in the epithelium for IFNα and IFNγ responses: (**G**) IFNα and (**H**) IFNγ in the incidental group vs. matched FT.I; (**I**) IFNα and (**J**) IFNγ in the cancer group vs. matched FT.C. The early upregulation of key IFNα– and IFNγ–induced genes such as *STAT1*, *ISG15*, *IFITM1*, *IRF7*, *IRF9*, and *HLA-A* at the p53.I stage, relative to matched FT.I, indicated early IFN pathway activation in HGSOC progression. In the heatmaps, columns represent individual genes and rows represent lesion types. Values show the median of the posterior distribution from the Bayesian analysis. Significance was determined based on the highest density interval relative to the region of practical equivalence (0.05 times the SD). Comparisons with >95% of the highest density interval outside the region of practical equivalence were significant (*), and >99% were very significant (**; ref. 111).

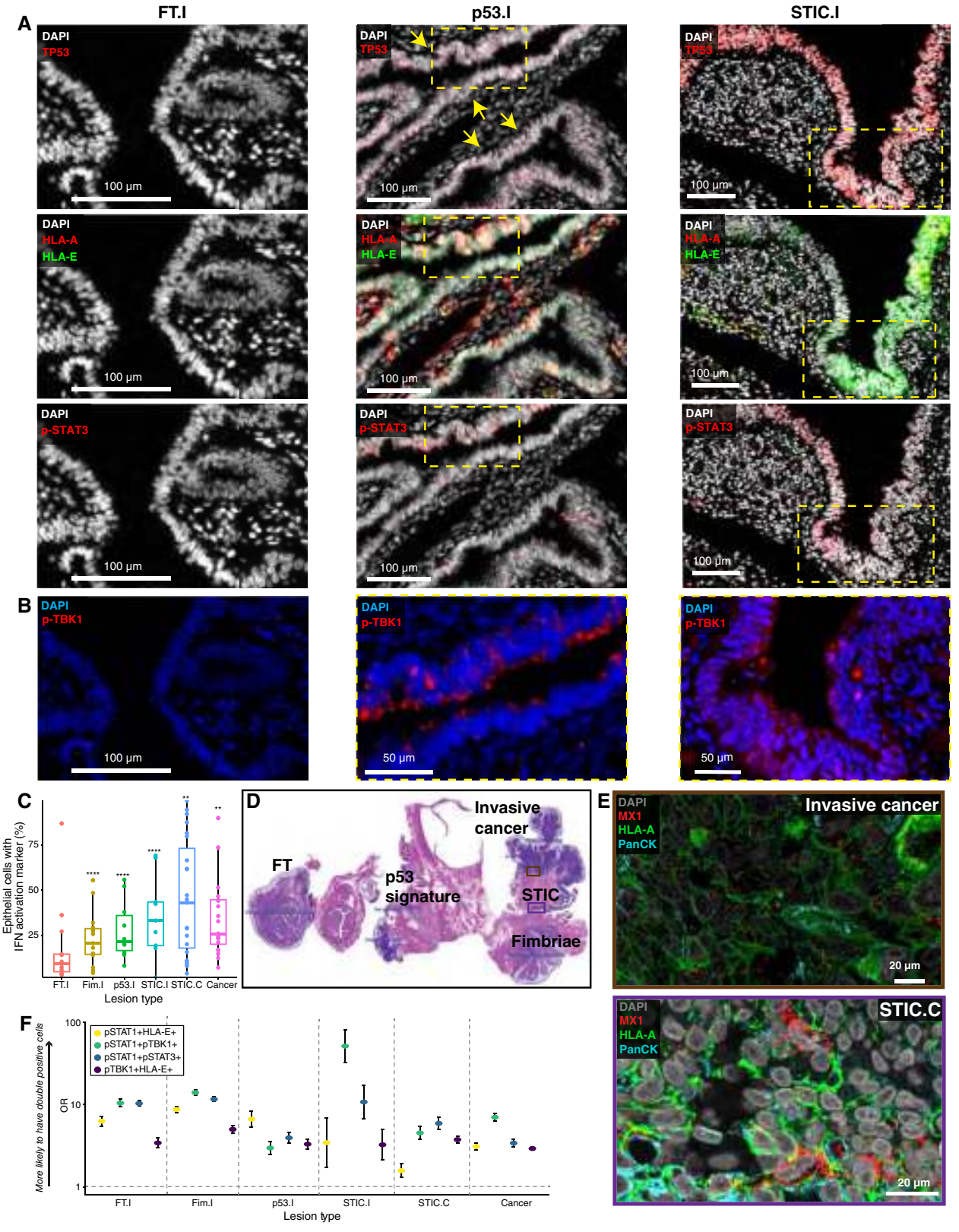

Figure 3. Multiplexed tissue imaging revealed spatially coordinated IFN in HGSOC progression. **A,** CyCIF images highlight markers indicating downstream IFN pathway activation, including of MHC class I (HLA-A and HLA-E) and phosphorylated STAT3 (p-STAT3), in both p53.I and STIC.I lesions. The representative STIC.I images are shown with the matched FT.I region from the same patient [case CD302.04(939), patient ID 40, *BRCA* WT], whereas the p53.I image is from a different patient [case C21-22 patient ID 28, *BRCA1* mutant (Mut)]. Yellow arrows in the p53.I image (*continued on following page*)

However, deconvolution analysis revealed that both precancer (precursor) and cancer ROIs are enriched for cancer-related EMT genes, supporting the presence of EMT during precursor development and progression (Supplementary Fig. S5A–S5C). The TGF-β pathway is known to induce EMT and interact with the PI3K/mTOR or KRAS pathways (39), both of which were activated before or during the STIC.C stage (Fig. 2B and C), potentially promoting growth even at early stages. Compared with precursor lesions, established cancer displayed enrichment for genes associated with Hedgehog signaling and angiogenesis pathways (Fig. 2D). Analysis of the stromal compartment surrounding HGSOC precursors and cancer revealed a similar trend. In early stages, the stroma displayed enrichment for IFN response and IL6–JAK–STAT3 signaling pathways (Supplementary Fig. S6A–S6D), suggesting these pathways play a role during early stages of disease, likely through immune modulation and paracrine signaling.

RNA Analysis Shows Early Persistent IFNα/γ Activation, IFN-Related DNA Damage Resistance Signature Emergence, and IFNε Signaling Downregulation in Later Stages

As GSEA indicated early activation of the IFN response in HGSOC progression (starting at the p53.I stage), we performed a more detailed analysis of this pathway. We examined specific gene sets related to IFNα, IFNγ (35), IFN-related DNA damage resistance signature (IRDS; refs. 40, 41), and IFNε (Supplementary Table S3; Supplementary Fig. S6E–S6H; refs. 42, 43). Because of the complex molecular relationships between disease stages, data variability, and patient-to-patient variation, we used a Bayesian ordinal regression model (44) to analyze gene expression changes across disease stages (Fig. 2E and F).

The model confirmed a significant upregulation of key IFNα/γ pathway genes in p53 signatures (p53.I), STIC lesions (STIC.I and STIC.C), and established cancer compared with matched normal epithelium (Fig. 2G–J). This activation included significant upregulation of *STAT1* (an upstream activator of IFN signaling) and IFN-induced and regulatory factors (*IFITM1*, *IRF9*, and *IRF7*), with *IFITM1* induced even in the Fim.I stage (Fig. 2G and H). IFN-stimulated genes (such as *ISG15*) were also elevated, along with genes involved in antigen processing and presentation (*TAP1* and *HLA-A*; Fig. 2G and H). Prior studies have shown that elevated type-I IFN activation results in the upregulation of classical MHC genes, including *HLA-A*, *HLA-B*, and *HLA-C*. The nonclassical MHC class gene *HLA-E*, often coexpressed with *HLA-A* upon IFNγ activation (45–50), plays additional immune regulatory roles. Upregulation of key IFNα/γ pathway genes persisted in STIC.C and cancer cells (Fig. 2I and J). Furthermore, both classical (*HLA-A/B/C*) and nonclassical (*HLA-E*) MHC class I antigen presentation molecules were upregulated in the epithelial compartment of p53.I and STIC.I lesions (Supplementary Fig. S6I). Collectively, these findings highlight a robust and sustained induction of IFNα/γ pathway genes that persists throughout HGSOC development, underscoring a potential role in disease progression.

Recent studies have shown that the female reproductive tract epithelium, including the FT epithelium, constitutively expresses IFNε, a type-I IFN, for immune defense (42, 43, 51, 52). Our data revealed a significant decrease in *IFNE* (i.e., IFNε transcript expression), *IFNA2*, and *IFNA4* expression, in STIC.C and cancer epithelium compared with matched normal epithelium (Supplementary Fig. S6E and S6F). However, downregulation of IFNε signaling was not observed in incidental precursors, suggesting it occurs later in HGSOC progression, after the initial IFNα and IFNγ response.

Chronic activation of the IFN pathway, known as IRDS, has been linked to chemotherapy and radiotherapy resistance in various cancers (40, 41, 53). Upregulated IRDS genes included *STAT1*, *MX1*, and the antiapoptotic BCL-2 family member *MCL1* in STIC.C and cancer, with a trend toward increased expression in STIC.I (Supplementary Fig. S6G and S6H). Persistent IFN activation might contribute to the emergence of IRDS, particularly during the later stages of STIC clonal expansion. Overall, the data suggests dynamic shifts in IFN signaling throughout HGSOC progression. Early activation of IFN during the p53 signature stage persists and intensifies as the disease progresses, coinciding with the downregulation of IFNε signaling and the emergence of IRDS. These findings indicate a potential link between sustained IFNα/γ activation, clonal selection, and the gradual accumulation of tumor-promoting and immune-suppressive pathways.

Figure 3. ***(Continued)*** indicate the epithelial cell layer exhibiting a "p53 signature." **B,** CyCIF images show that phosphorylated TBK1 (p-TBK1) appears as cytosolic, punctate signals in the same regions in which HLA-A, HLA-E, and p-STAT3 are expressed. The FT.I, p53.I, and STIC.I areas are identical to those in **A**, with ROIs for p53.I and STIC.I indicated by yellow boxes in **A**. The coexpression of these markers suggests that p-TBK1 signaling may be an upstream event driving IFN pathway activation. **C,** A box plot illustrates the increasing percentage of epithelial cells expressing IFN activation–associated markers (p-TBK1$^+$/p-STAT1$^+$/HLA-E$^+$/p-STAT3$^+$) as disease progresses. The sample sizes per lesion type are as follows: FT.I ($n = 13$), Fim.I ($n = 15$), p53.I ($n = 10$), STIC.I ($n = 9$), STIC.C ($n = 23$), and cancer ($n = 20$). The median is represented by a solid line, with whiskers extending to 1.5 times the IQR. Statistically significant differences compared with FT.I are indicated by asterisks; **, $P < 0.001$; ****, $P < 0.0001$. Binomial generalized LMM with patient ID as random effect were used. The model formula was cbind(n_success, n_failure) ~ stage + (1 + stage|patient_id) using the lme4 R package (version 4.3.3). Summary statistics are in Supplementary Tables S5 and S6. **D,** H&E image of a whole-slide specimen (case RD-23-002, patient ID 9, *BRCA2* mutant, stage IC HGSOC) indicating the ROIs used in **E**. This specimen, also shown in Fig. 1F, contains all histologic elements described and was used in high-resolution 3D CyCIF performed on a thicker section from the same block. Figure 1F (H&E) and Figs. 3D and 4B (3D CyCIF H&E) show the same H&E-stained section to provide orientation in different imaging contexts. **E,** A 3D CyCIF reconstruction of a STIC with concurrent HGSOC (patient ID 9, ROIs from **D**). MX1, an IFN-induced gene, shows punctate expression and is coexpressed with PanCK and HLA-A, indicating IFN activation in both tumor and STIC.C epithelial cells. **F,** A plot showing the OR for coexpression of various protein pairs (p-STAT1$^+$ HLA-E$^+$ or p-STAT1$^+$ p-TBK1$^+$ or p-STAT1$^+$ p-STAT3$^+$ or p-TBK1$^+$ HLA-E$^+$) across different disease stages. OR > 1 indicates increased likelihood of coexpression, whereas an OR < 1 indicates decreased likelihood. The *Y*-axis is on a $\log_{10}$ scale. Single cells were classified as positive or negative for each marker, and contingency tables were constructed to compute ORs using generalized LMMs. All lesion types demonstrated significant marker coexpression ($P < 0.001$). Fisher exact tests yielded comparable ORs. See Supplementary Tables S5 and S6 for summary statistics. PanCK, pan-cytokeratin.

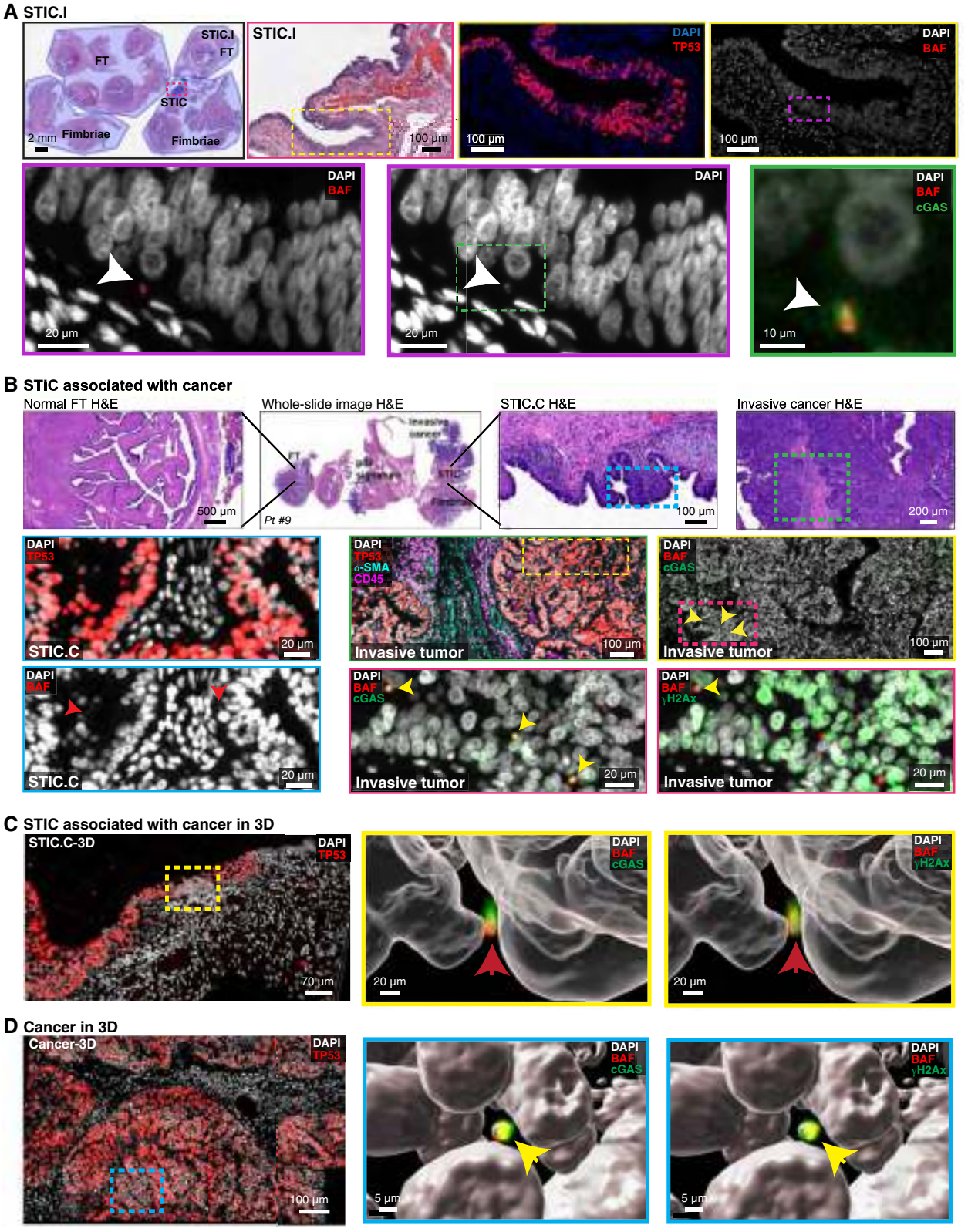

Figure 4. Tissue imaging reveals micronuclear rupture and cGAS recruitment in HGSOC progression. **A,** Top, An H&E image of a representative STIC.I case [CD302.03(706), patient ID 38, *BRCA1* mutant (Mut)], with ROIs indicated. Within the STIC region outlined by a purple box, CyCIF imaging shows TP53-positive epithelial cells containing BAF staining. Bottom, Colocalization of BAF signal with DNA (DAPI) marks a ruptured micronucleus (MN; white arrowheads). A higher magnification view (outlined by a green box) confirms the colocalization of cGAS at BAF-positive MN, (*continued on following page*)

Multiplexed Imaging Reveals Spatially Coordinated IFN Signaling in HGSOC Progression

CyCIF is a multiplexed imaging technique that quantifies protein marker expression at a single-cell level (54). We used CyCIF to visualize IFN pathway activity within HGSOC precursors. This analysis revealed a stepwise increase in the number of epithelial cells expressing IFN pathway markers (e.g., p-TBK1, p-STATs, and HLA-A/E) across disease stages (p53.I: median 22%, STIC.I: 33%, STIC.C: 43%, and cancer: 26%) regardless of *BRCA* mutation status (Fig. 3A–C; Supplementary Figs. S7A–S7C, S8A, S8B, and S9A–S9F). Ciliated cells in the normal FT showed high levels of STING protein but no evidence of IFN pathway activation (Supplementary Fig. S9G–S9J), consistent with a prior report (55). High-resolution 3D CyCIF imaging of STIC.C and invasive cancer confirmed co-expression of the IFN-inducible protein, MX1, which formed multiple discrete puncta, and the antigen-presenting protein HLA-A within epithelial cells (pan-cytokeratin$^+$; Fig. 3D and E), reconfirming IFN induction in MHC class I–expressing epithelial cells.

Despite the observed increase in IFN marker expression with disease progression, there was significant inter- and intra-sample heterogeneity of IFN pathway markers across all stages (Supplementary Figs. S2A, S8A, S8B, and S10–S12). For instance, within the same STIC.I lesion, we observed both HLA-E–positive and HLA-E–negative cells (Supplementary Fig. S2A). In cancer, we also noted variability in the intensity of IFN pathway marker expression, such as the presence of both HLA-E low- and high-intensity tumor regions within the same patient (Supplementary Fig. S11). We leveraged this heterogeneity to explore the potential for localized and coordinated IFN signaling in HGSOC precursors. Visual inspection of CyCIF images suggested coexpression of IFN markers within individual cells (Fig. 3A, B, and E; Supplementary Figs. S7A–S7C and S10). This observation was further supported by pairwise correlation analysis, which demonstrated strong positive correlation between various pairs of IFN markers (e.g., pSTAT1$^+$ HLA-E$^+$; p-STAT1$^+$ p-TBK1$^+$; pSTAT1$^+$ p-STAT3$^+$; and p-TBK1$^+$ HLA-E$^+$) across all disease stages (OR 1.5–50, Fig. 3F). Whereas the percentage of cells expressing IFN markers (e.g., HLA-E) was relatively low at early stages (p53.I median: 4%), it increased in STIC.I (16%), STIC.C (26%), and invasive cancer (18%; Supplementary Fig. S9C). The high probability of IFN marker coexpression suggests coordinated and localized activation of the IFN pathway throughout HGSOC development. The progressive increase in IFN-positive cells within precursor lesions further implies clonal expansion driven by positive selection during disease progression.

Interplay between HLA-E expression, the IFN Pathway, and Immune Evasion Mechanisms

Loss of classical MHC class I is a well-established mechanism of immune evasion in cancers, including advanced HGSOC (56, 57). However, tumors may become vulnerable to NK cell–mediated killing when nonclassical MHC class I HLA-E is lost (46, 58, 59). Conversely, overexpression of HLA-E in various cancers, including cervical and ovarian cancer, allows tumor cells to evade NK cell surveillance (46, 48, 60–62), likely contributing to the development of more aggressive tumor (49, 60–62). To investigate the relationship between HLA-E expression and transcriptional programs, we categorized the GeoMx ROIs based on HLA-E protein expression (imaged by CyCIF in serial tissue sections) into HLA-E–positive or HLA-E–negative groups (Supplementary Fig. S2A; Supplementary Table S2). As expected, analysis of differentially expressed genes showed a significant upregulation of the *HLA-E* gene itself in ROIs positive for HLA-E protein (e.g., from STIC.I, Supplementary Fig. S13A). Interestingly, in early STIC lesions (STIC.I), HLA-E positive regions showed enriched expression of genes related to cell morphology and migration (*ARAP2*), antigen presentation (*HLA-A*, *HLA-B*, *HLA-DRA*, *HLA-DQB1*, *HLA-F*, *TAP*, and *TAPBP*), coagulation (*F5*), and complement pathways (*CFB*, *CFH*, *CFI*, *C1S*, *C2*, and *C4B*), suggesting a coordinated inflammatory and tissue remodeling response. Cell growth and maturation pathways were also induced, including the *MYC* oncogene, as were downstream IFN genes (*MX1*, *IRF1*, *DDX60*, *OAS3*, *IFI44*, *PSMB8*, and *XAF1*). Further analysis using Bayesian modeling with HLA-E status as a covariate showed a strong association of HLA-E–positive epithelial ROIs with IFN responses (type I and II; IFNα/γ) and IRDS, as early as the p53.I stage (Supplementary Figs. S13B, S13C, S13D, and S14A–S14G). Differential gene expression and GSEA analysis further supported this association across disease stages (Supplementary Figs. S13C, S13D, S15A, S15B, S16A, and S16B). These findings suggest a complex interplay between HLA-E expression, IFN signaling, and various immune evasion mechanisms, potentially supporting early tumor development and progression.

In contrast to IFN pathway activation, genes associated with other well-established tumor-promoting pathways, such as TGF-β, EMT, and those characteristic of the aggressive C5/PRO subtype of HGSOC (Supplementary Table S3; refs. 22, 23), emerged primarily at the STIC.C and cancer stages (Supplementary Fig. S16C and S16D). Notably, these pathways were not restricted to HLA-E–positive epithelial areas. Further analysis of individual EMT-related genes (e.g., *CLDN6*, *CDH3*, *COL4A1*, *MMP14*, and *MMP2*) confirmed that increased expression at later stages was not limited to HLA-E–positive cells

Figure 4. ***(Continued)*** suggesting that cGAS binds to DNA from the ruptured MN. **B,** Top, H&E images of a representative STIC with concurrent HGSOC (case RD-23-002, patient ID 9, *BRCA2* mutant, stage IC HGSOC), previously shown in Figs. 1F and 3D, highlighting ROIs representing different histologies. A cyan box on the STIC.C H&E and a green box on the invasive tumor H&E indicate ROIs for panels below. Bottom, CyCIF images from the STIC.C region (left column) reveal BAF-positive MN (red arrowheads). Corresponding CyCIF images from the invasive cancer region (right columns) demonstrate an increased number of in BAF$^+$ cGAS$^+$ or BAF$^+$ γ-H2Ax$^+$ MN (yellow arrowheads), indicating more frequent MN rupture events in invasive disease. **C** and **D,** The same specimen from **B** was imaged using 3D confocal multiplexed imaging to confirm both intact and ruptured MN. **C,** A 3D reconstruction and surface rendering of a 20-μm-thick section confirms colocalization of BAF$^+$ and cGAS$^+$ in MN, as well as BAF$^+$ and γ-H2Ax$^+$ in MN in STIC.C (red arrowheads, yellow box). **D,** In the invasive cancer region, 3D multiplexed imaging revealed BAF$^+$ γ-H2Ax$^+$ MN rupture events (yellow arrowheads, cyan box). The colocalization of cGAS with BAF-positive MN suggests that cGAS recognizes DNA from ruptured MN.

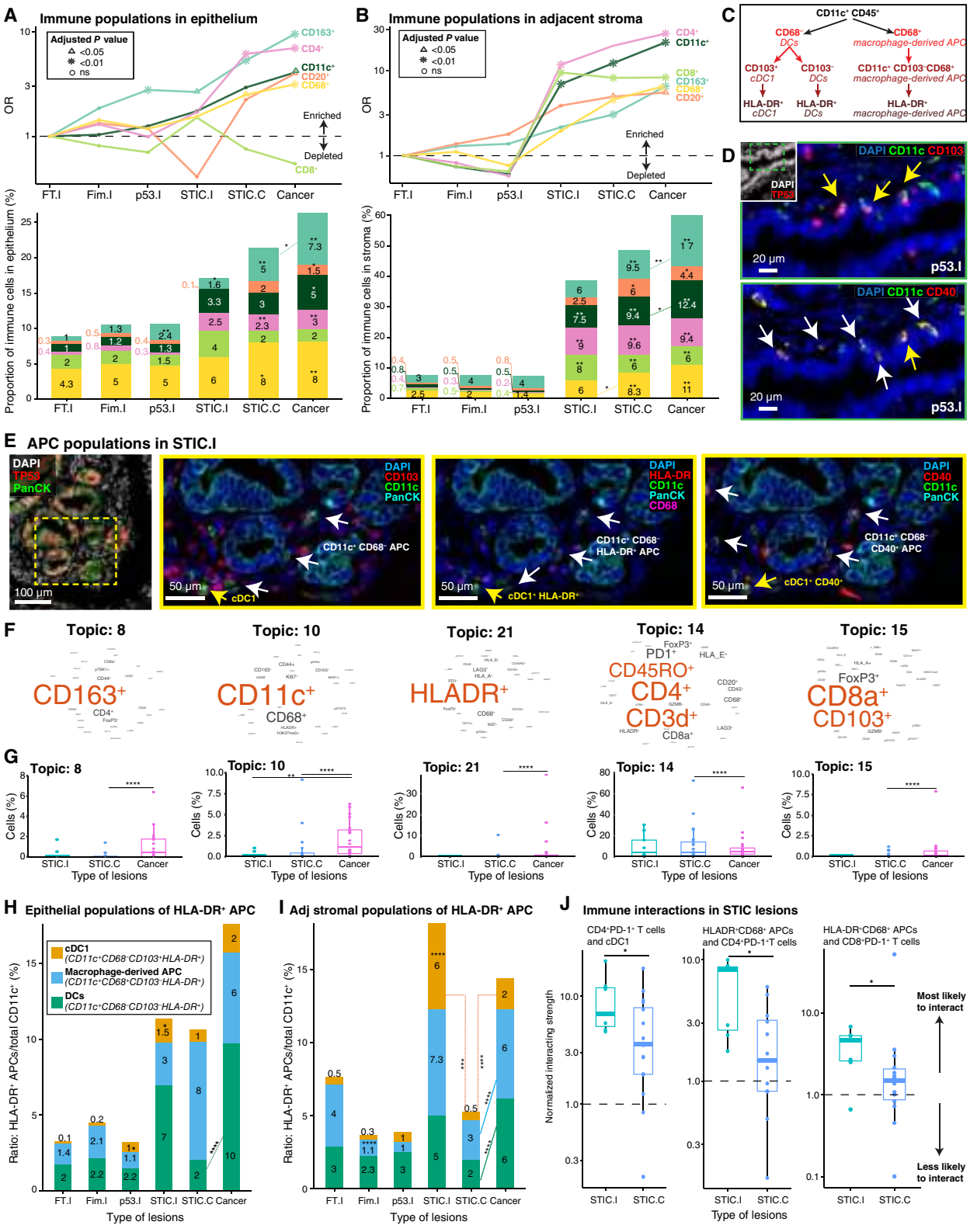

Figure 5. Immune composition analysis suggests active immune surveillance by activated antigen presenting cells at early HGSOC progression. **A** and **B**, Top, Line plots show changes in the proportions of major immune cell types across disease stages, based on single-cell CyCIF data. **A**, Epithelium and (**B**) adjacent stroma. The *Y*-axis shows Odds Ratios (ORs) relative to FT.I on a log scale, calculated using binomial GLMMs, with patient ID and observation-level random effects. *P* values are adjusted using the Benjamini–Hochberg procedure. Bottom, Stacked bar plots represent the average proportion of major immune cell types disease stages in the epithelium (**A**) and adjacent stroma (**B**). Asterisks on bars indicate (*continued on following page*)

(Supplementary Fig. S17). This suggests that additional tumor-promoting mechanisms, independent of the IFN pathway, likely play important roles in shaping HGSOC development.

Micronuclear Rupture and cGAS Recruitment in HGSOC Progression

The presence of an IFN response and p-TBK1$^+$ epithelial cells in early HGSOC precursors suggests activation of the cGAS-STING signaling pathway (63–65). This pathway responds to cytosolic DNA from various sources, including DNA damage, CIN, or LINE-1 open reading frame 1 protein expression (64, 66–69). CIN, a hallmark of advanced HGSOC (3, 70), can lead to the formation and rupture of MN containing missegregated chromosomes (65, 71, 72), which is linked to the presence of *TP53* mutations (73). We used CyCIF to identify p53$^+$ precursor lesions and assessed the presence and integrity of MN using barrier-to-autointegration-factor (BAF; *BANF1*), a sensitive marker for cytosolic DNA (Coy and colleagues, bioRxiv 2023; https://www.biorxiv.org/content/10.1101/2023.11.07.566063v1). Strikingly, BAF$^+$ MN ruptures were observed as early as STIC.I lesions, with increasing frequency in invasive cancer. Visual inspection revealed that a subset of ruptured MN contained cGAS, and some also contained the DNA damage marker γ-H2Ax (Fig. 4A and B; Supplementary Fig. S18A). High-resolution 3D CyCIF confirmed the colocalization of BAF, cGAS, and γ-H2Ax, with the highest frequency observed in invasive HGSOC (Fig. 4C and D; Supplementary Video; Supplementary Fig. S18B and S18C). These findings suggest that CIN-induced MN ruptures occur unexpectedly early in HGSOC and are associated with IFN signaling, possibly via cGAS-STING activation.

Spatial Organization of Immune Cells in HGSOC Development

Activation of the cIFN response plays a critical role in shaping the spatial organization and function of the immune system within the TME (64, 74). To investigate how the spatial organization of immune cells changes during HGSOC development, we first used CyCIF data to quantify major immune cell types in precursor lesions and invasive cancer (Fig. 5A–C). These cell types included (i) antigen-presenting cells (APC), such as cDC1 and macrophage-derived APCs, (ii) CD68$^+$ macrophages (M1-like), (iii) CD163$^+$ macrophages (M2-like), (iv) CD20$^+$ B cells, (v) CD4$^+$ T cells, and (vi) CD8$^+$ T lymphocytes (Fig. 5A–E). A minor population of NK cells was also detected (Supplementary Fig. S19A–S19G).

We then applied latent Dirichlet allocation (LDA), a statistical method for topic modeling, to analyze the spatial patterns of the immune microenvironment. LDA has been successfully used to reveal recurrent cellular neighborhoods in both precancer and cancer tissues (54, 75, 76). Based on cell type and activation markers, 4.22×10^7 single cells from 44 specimens were classified into 21 distinct groups, revealing recurrent local cellular neighborhoods ("topics"). These topics represent niches of specialized cell types or interacting cell types that may play a role in disease progression or response to therapy. Several notable recurrent neighborhoods were identified, including topic 8, which predominantly comprised CD163$^+$ (M2-like) macrophages, topic 10, dominated by CD11c$^+$ APCs, and topic 21, characterized by HLA-DR$^+$ (activated) APC cells (Fig. 5F). Each of these neighborhoods was significantly enriched in invasive cancer compared with STIC lesions (Fig. 5G). Topic 14 displayed high levels of CD4$^+$ T cells, whereas topic 15 contained both CD8$^+$ T lymphocytes (including CD103$^+$ T_{RM} cells) and FOXP3 T regulatory (Treg) cells. These T cell–rich neighborhoods were also more prevalent in invasive cancer compared with STIC lesions (Fig. 5F and G). These findings suggest that HGSOC progression involves dynamic reorganization of immune cell spatial distribution, potentially influencing cell type interactions, immune signaling, and the overall antitumor immune response.

cDC1 and NK Cells Decrease Whereas Macrophages Increase in Later Stages of HGSOC Development

We next used the CyCIF and GeoMx datasets to better understand how the organization of specific immune cell subtypes changes during different stages of HGSOC progression. We first focused on two cell types that are critical organizers of the initial immune response to tumors: cDC1 (CD11c$^+$, CD103$^+$, and CD68$^-$; refs. 58, 77, 78) and NK cells (NKG2D$^+$ CD3$^-$). Intratumoral NK cells produce chemokines that recruit cDC1 into the TME, whereas cDC1 cells transport tumor antigens to lymph nodes to promote CTL responses.

Figure 5. ***(Continued)*** significant differences vs. FT.I; asterisks between bars (dashed lines) indicate significant inter-stage differences. *, $P < 0.05$; **, $P < 0.01$. Average proportions were rounded up to the next whole number when applicable and shown for each cell type across lesion types. Sample sizes: FT.I ($n = 13$), Fim.I ($n = 15$), p53.I ($n = 10$), STIC.I ($n = 9$), STIC.C ($n = 23$), and cancer ($n = 20$). **C,** Schematic illustrating subsets of CD11c$^+$ cells identified by CyCIF, including cDC1, and other APCs. Activated APCs are characterized by HLA-DR$^+$ expression (MHC class II), marking an initial step of APC activation. **D,** CyCIF image from a representative p53.I case [also shown in Fig. 3A; case C21-22 patient ID 28, *BRCA1* mutant (Mut)] highlights an epithelial region with "p53 signature" (green box). This region contains activated APCs, including cDC1 (yellow arrows) and other DCs (white arrows), identified by CD40$^+$ CD11c$^+$ staining. **E,** CyCIF image from a STIC.I case [CD302.03(706), patient ID 38, *BRCA1* mutant (Mut)]. The yellow box marks an area of activated APCs, including cDC1 (yellow arrow) and other DCs (white arrows) in the stroma adjacent to the STIC.I epithelium. Pan-cytokeratin (PanCK) and TP53 staining highlight the epithelial cells. **F,** LDA neighborhood analysis applied to multiplex tissue imaging. Frequencies from all incidental and cancer samples were pooled to train the LDA model. Each "topic" represents a cellular neighborhood defined by distinct immune cell types and states. Font size reflects prevalence in LDA components. Detailed topic descriptions are in Supplementary Table S5. **G,** Box plots depicting the percentage of cells in each LDA topic across STIC.I, STIC.C, and cancer stages. The number of specimens for each lesion is as follows: STIC.I ($n = 9$), STIC.C ($n = 23$), and cancer ($n = 20$). Significant differences are indicated by asterisks; **, $P < 0.01$; ****, $P < 0.0001$ using generalized LMMs with patient ID as a random effect. **H,** Stacked bar plot of the average proportion of HLA-DR$^+$ APC subsets within the total CD11c+ population in the epithelium across lesion types. **I,** Similar plot for the adjacent stroma. **H** and **I,** Proportions are rounded to the nearest whole number where applicable. Number of specimens per group as follows: FT.I ($n = 13$), Fim.I ($n = 15$), p53.I ($n = 10$), STIC.I ($n = 9$), STIC.C ($n = 23$), and cancer ($n = 20$). Asterisks indicate significant differences from FT.I or between groups. *, $P < 0.05$; ****, $P < 0.0001$, using binomial generalized LMMs with patient ID as a random effect. **J,** Box plots illustrating normalized interaction strength (on a $\log_{10}$ scale) between cell types in STIC.I and STIC.C: (i) cDC1 and CD4$^+$ PD1$^+$ T cells, (ii) HLA-DR$^+$ CD68$^+$ APCs with CD4$^+$ CD8$^+$ PD-1$^+$ T cells, and (iii) HLA-DR$^+$ APCs with CD8$^+$ PD-1$^+$ T cells. Scores >1 indicate stronger interactions in STIC.C vs. STIC.I. Significance is indicated by asterisks; *, $P < 0.05$, Wilcoxon rank-sum test.

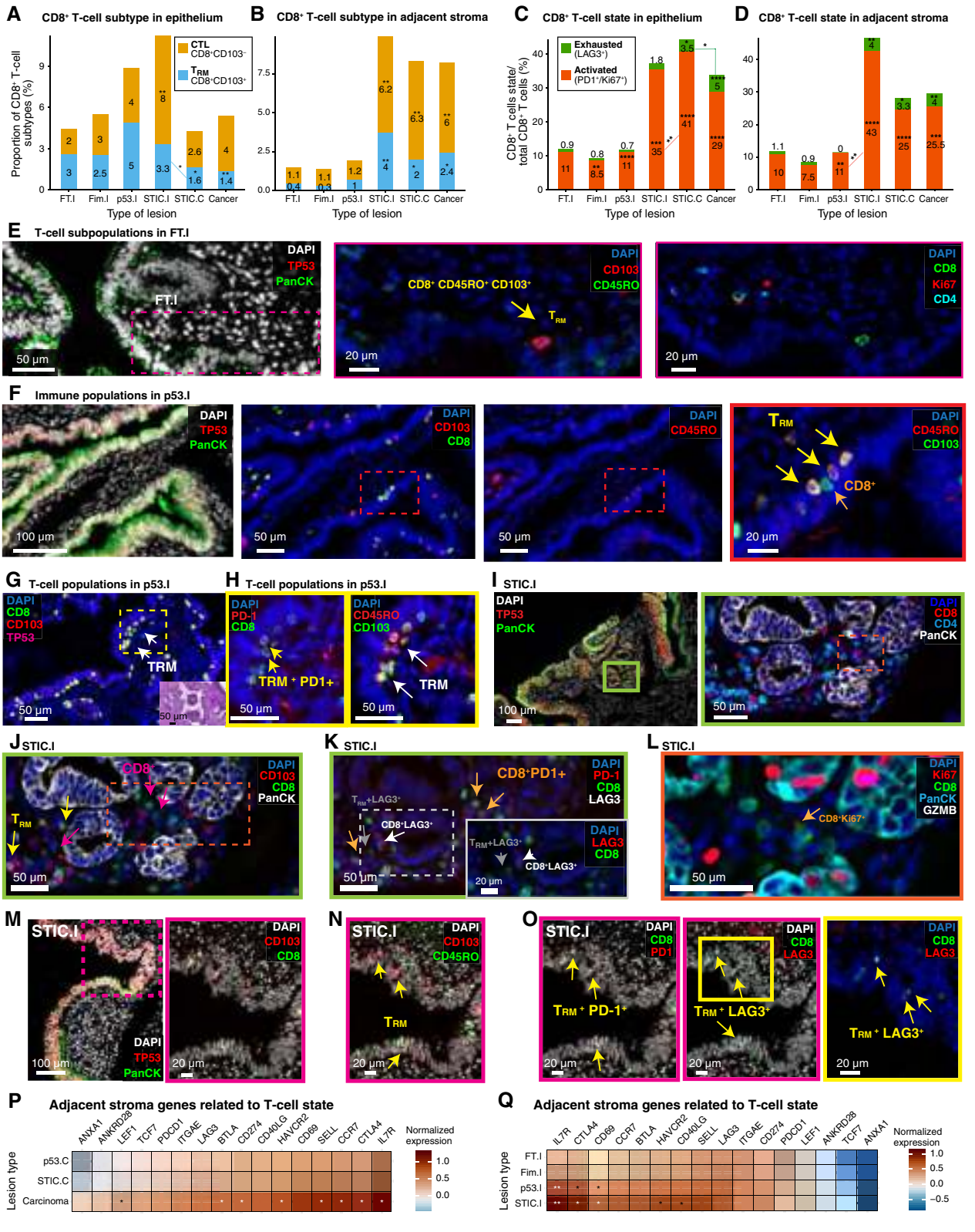

Figure 6. Immune editing and T-cell dysfunction at early stage of HGSOC development. **A** and **B,** Stacked bar plots summarize CD8+ T-cell subtypes identified by CyCIF across disease stages in the epithelium (**A**) and in the adjacent stroma (**B**). Subtypes include T_{RM} cells (CD8+ CD103+ CD45RO+) and cytotoxic T cells (CTLs; CD8+ CD103−). Sample sizes: FT.I ($n = 13$), Fim.I ($n = 15$), p53.I ($n = 10$), STIC.I ($n = 9$), STIC.C ($n = 23$), and cancer ($n = 20$). Black asterisks show significant differences vs. FT.I, whereas colored dashed lines with asterisks indicate significant intergroup comparisons; *, $P < 0.05$; **, $P < 0.01$, determined by binomial generalized LMMs with patient ID and observational level random effect. **C** and **D,** Stacked bar (*continued on following page*)

cDC1 cells have superior antigen processing and presentation capacities, making them highly effective in activating and recruiting CD8+ CTLs (77, 79–82). Using CyCIF imaging, we observed that, although the total population of CD11c+ APCs (which includes cDC1 cells) increased with disease progression (Fig. 5A and B), the number of HLA-DR+ cDC1 cells (indicating antigen-presenting function) rose significantly in the early stages, particularly in the epithelium (Fig. 5C and H). These cells were 10-fold more abundant in p53.I epithelium and 15-fold higher in STIC.I epithelium compared to normal epithelium but remained relatively stable with disease progression. In the stroma, cDC1 populations expressing HLA-DR increased 12-fold in STIC.I compared with normal tissues but decreased substantially in more advanced lesions (12-fold decrease in STIC.C and 3-fold in established cancers compared with STIC.I; Fig. 5I). This suggests that the antigen-presenting function provided by cDC1 decreases as precursor lesions progress. Similarly, NK cells, which were present at low levels in normal tissue and p53.I precursors (median 0.1%), became nearly undetectable in later stages of the disease (STIC.I, STIC.C, and cancer; median: 0.02%; Supplementary Fig. S19A and S19B), indicating a further decline in antitumor immunity.

To validate these findings, we performed Bayesian modeling of the spatial transcriptomic data to analyze gene sets specific to cDC1 and NK cells (Supplementary Table S3; refs. 58, 77, 78). This analysis confirmed the CyCIF findings, showing that cDC1 and NK cells are present in early precursors but decrease with disease progression, particularly in STIC.C and tumor stages. Later-stage lesions showed reduced gene expression related to cDC1 function and NK–cDC1 axis activity. These genes included *CLEC9A*, *BATF3*, *CLNK*, *XCL1*, *XCR1*, *IL15*, and *IL12*. In addition, genes associated with NK cell receptors, such as *KLRK1*, *NCR1*, and *CD226* (which encode NKG2D and activation receptors NKp46 and DNAM1, respectively), also declined. There was also a decrease in genes related to NK inhibitory receptors, including *KLRD1* (CD94), *KLRC2* (NKG2A/C), and *KLRG1*, as well as *KIR*s (Supplementary Fig. S20A and S20B). These demonstrate progressive dysfunction of NK and T cells in STIC.C and tumor epithelium, supported by decreased expression of genes related to cytotoxic activity, such as *PRF1*, *NKG7*, *GZMB*, *GZMK*, *GZMH*, and *GZMA* (Supplementary Fig. S20C–S20F). Considered together, these findings suggest a suppression of NK cell and cDC1 activity during HGSOC development.

Whereas NK cells and cDC1 decline during HGSOC development, tissue imaging revealed a stepwise increase in macrophage populations with disease progression, as suggested by LDA analysis topic 8 (Fig. 5F and G). Both CD68+ M1-like macrophages and CD163+ M2-like macrophages became more abundant, reaching their highest levels in invasive cancer (Fig. 5A and B; Supplementary Fig. S21A and S21B). Interestingly, more than 50% of CD68+ cells coexpressed CD11c, suggesting they function as APCs [i.e., macrophage-derived APCs (79); Supplementary Fig. S21C and S21D]. These macrophage-derived APCs frequently coexpressed HLA-DR (83) and/or CD40, which are markers of antigen presentation and T-cell costimulation (Fig. 5D, E, H, and I; Supplementary Fig. S21E–S21H). For comparison, less than 1% of epithelial cells in precursor lesions or tumor expressed HLA-DR (Supplementary Fig. S22A–S22I). Spatial transcriptomic data provided further support for an increase in APCs with disease progression. Whereas multiple cell types can produce various chemokines and cytokines (e.g., *CXCL9*, *CCL3*, and *TNF*), the data showed an increasing trend of gene expression associated with both M1 and M2 macrophages (84) in the cancer group, including stabilin-1 (*STAB1*), *AXL*, *IL10*, and *CD163* (Supplementary Fig. S23A–S23H). Moreover, there was an increase in the expression of MHC class II (*HLA-DRA*, *HLA-DMA*, and *HLA-DRB1*) in the stroma of precursors and invasive cancer (Supplementary Fig. S23I and S23J). Taken together, these findings suggest an increase in macrophage-derived APCs that express HLA-DR, especially in cancer, indicating that these cells may play a role in presenting tumor antigens to CD4+ T cells.

Shifting Functional Landscape of CD4+ T Cells in HGSOC Development

The observed changes in APC composition during HGSOC progression—a decrease in cDC1 and an increase in macrophage-derived APCs—led us to further characterize CD4+ T cells, which are critical partners for APCs in orchestrating

Figure 6. ***(Continued)*** plots showing the proportion of CD8+ T-cell states within total CD8 T cells in the epithelium (**C**) and the adjacent stroma (**D**). T-cell states are defined as activated (Ki67/PD-1+ and LAG3−) and exhausted (PD-1+LAG3+ or LAG3+). Same specimen counts as above. Significance levels from FT.I are marked by black asterisks stages; *, $P < 0.05$; ***, $P < 0.001$; ****, $P < 0.0001$, using binomial generalized LMMs. Colored dashed lines indicate significant intergroup comparisons. **E,** CyCIF images from a representative FT.I case matched to STIC.I [case CD302.04(939), patient ID 40, *BRCA* WT; also shown in Fig. 3A]. A T_{RM} cell (CD8+ CD103+ CD45RO+) is indicated by a yellow arrow. **F,** CyCIF image from a representative p53.I case [case C21-22 patient ID 28, *BRCA1* mutant (Mut); also shown in Fig. 3A]. The red box marks a "p53 signature" – T_{RM} (yellow arrows) and CD8+ CD103− CTL (orange arrow) are seen at higher magnification. Different markers from the same specimen are shown in multiple figures, enabling direct comparisons. **G** and **H,** CyCIF images from another p53.I case (C21-80, patient ID 35, *BRCA2* Mut), displaying T_{RM} (white arrows) coexpressing PD-1 (yellow arrows). **I** and **J,** CyCIF images from a representative STIC.I case, also shown in Fig. 5E [CD302.03(706), patient ID 38, *BRCA1* Mut], showing CTL (magenta arrows) and T_{RM} (yellow arrows) within the stroma. **K,** CyCIF image of the same ROI as in **J**, illustrating T-cell exhaustion in STIC.I. PD-1 (orange arrows) and LAG3 (punctate expression) colocalize on CTL (white arrows) and T_{RM} (gray arrows). The inset provides a magnified view of the gray ROI for LAG3+ T cells. **L,** CyCIF image of the same STIC.I ROI indicated as in **I** and **J** showing a proliferative CD8+ T cell (CD8+ Ki67+ GZMB−; orange arrow). **M** and **N,** CyCIF images from another STIC.I case [CD302.04(939), patient ID 40, *BRCA* WT, also shown in Fig. 3A], highlighting TP53-positive epithelium (**M**) and T_{RM} cells in the STIC.I epithelium (**N**; yellow arrows). **O,** CyCIF images of same ROI as in **N**, showing exhausted intra-epithelial T_{RM} in STIC.I, coexpressing PD-1 and LAG3 (yellow arrows). **P** and **Q,** Heatmaps showing normalized gene expression related to various T-cell states (naïve, dysfunctional, and memory) in the stroma from the cancer group (**P**) and stroma from incidental group. (**Q**) Genes include *HAVCR2* (encoding TIM3), *CTLA4*, *PDCD1* (PD-1), *ITGAE* (CD103), *TCF7* (TCF1), and *CD274* (PD-L1). Rows represent lesion stages, and columns represent genes. Asterisks indicate significant changes from baseline stages (p53.C in **P** and FT.I in **Q**) based on an ordinal Bayesian modeling. Significance is defined by the proportion of the posterior highest density interval outside the region of practical equivalence (*>95%, **>99%). These findings underscore the early emergence of T-cell dysfunction and immune editing in HGSOC precursors such as STIC.I.

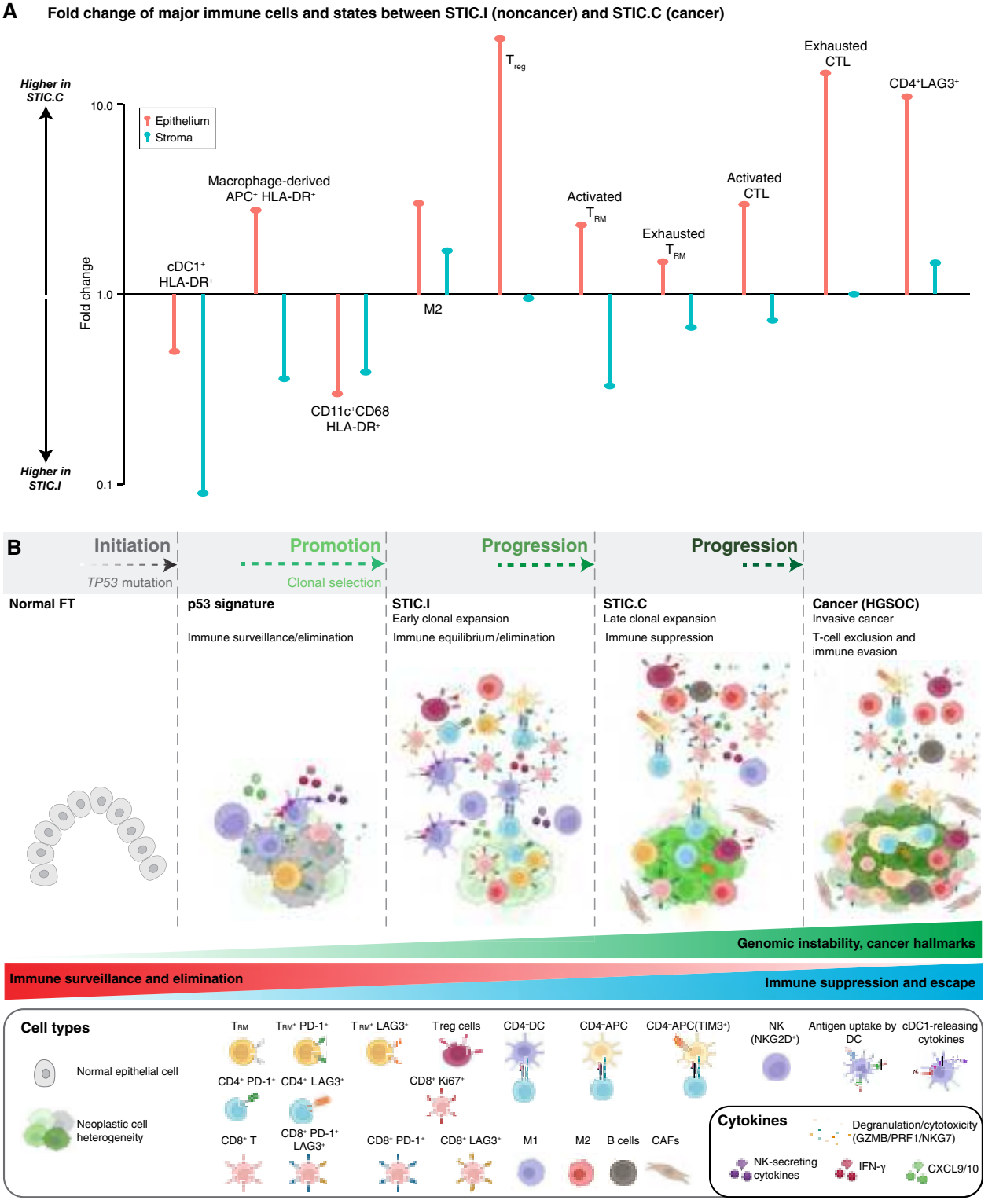

Figure 7. Evolution of the precancer ecosystem during HGSOC progression. **A,** A lollipop plot illustrates the relative differences in major immune cell types and states between STIC.I and STIC.C in both epithelial and stromal regions. The fold difference is computed as the ratio of the average proportion of each cell state in STIC.C compared with STIC.I. A value of 1 indicates no change, values >1 signify an increased prevalence in STIC.C, and values <1 indicate a higher prevalence in STIC.I. **B,** Schematic representation of HGSOC progression, emphasizing the temporal development of hallmark cancer features and the dynamic interplay and interactions between immune cells and precancer/cancer cells. Cancer often starts with oncogenic changes (mutations, aneuploidy, and other cancer hallmarks) under selective pressure. These cells may remain latent for decades. Only a subset of these "phenotypically normal" but mutated clones undergo clonal expansion and acquire additional mutations, ultimately developing (*continued on following page*)

adaptive immune responses. CyCIF analysis revealed a progressive increase in CD4+ T-cell infiltration throughout the disease course (Fig. 5A and B; Supplementary Fig. S24A and S24B). However, both activation and dysfunction markers were observed in these CD4+ T cells. More than 35% of CD4+ T cells expressed either HLA-DR or PD-1, suggesting potential antigen presentation and activation, starting from the STIC.I stage (Supplementary Fig. S24A and S24B). At the same time, the presence of numerous Tregs (CD4+ FOXP3+ Tregs: ~14%) and CD4+ LAG3+ (~14%) indicated the development of an immunosuppressive microenvironment and potential dysfunction of antigen presentation (Supplementary Fig. S24A and S24B).

CD4+ T-cell activation relies on antigen presentation by MHC class II molecules, primarily expressed by APCs. Whereas direct interactions between CD4+ T cells, HLA-DR-expressing APCs, and CD8+ T cells were observed, there was evidence of a dampening effect—some APCs coexpressed HLA-DR/CD40 along with TIM3, an inhibitory receptor that modulates the function of both lymphoid cells and APCs, suggesting a reduced capacity for antigen presentation (Supplementary Fig. S25A–S25C; refs. 85–88). Quantitative analysis comparing the cell–cell interactions in STIC.I and STIC.C lesions showed decreased proximity (normalized interaction score) between activated CD4+ T cells, CD8+ T cells, and cDC1/macrophage-derived APCs expressing HLA-DR in STIC.C lesions (Fig. 5J). Thus, whereas CD4+ T cells infiltrate HGSOC precursor lesions, their capacity for activation may be counterbalanced by the emergence of suppressive mechanisms, potentially contributing to disease progression.

CD8+ T Cell Dynamics and Dysfunction in Early HGSOC Development

We also observed changes in the numbers, activation states, and localization of CD8+ T cells within the tissues during HGSOC development. Compared with normal tissue, CD8+ T cells increased significantly in the epithelium of STIC.I lesions (2-fold) and even more dramatically in the stroma (10-fold; Fig. 5A and B). However, this increase was followed by a gradual decline in later disease stages (STIC.C and cancer), with a sharper decrease in CD8+ T-cell number in the epithelium as compared with the stroma (2-fold vs. 1.5-fold).

Many different CD8+ T-cell subsets were present, including T_{RM} cells (CD8+ CD103+ CD45RO+), a specialized subset of CD8+ T cells adapted for localized immune surveillance within specific tissues (89, 90), and conventional cytotoxic CD8+ CTLs (CD8+ CD103− CD45RO−). We used markers such as Ki67, PD-1, GZMB, TIM3, and LAG3 to assess their functional states (Fig. 6A–D). T_{RM} cells increased 1.5-fold in p53.I epithelium compared with normal epithelium but gradually decreased with disease progression (Fig. 6A, E, and F). CTL numbers started to rise in p53.I, with the most striking increase observed in STIC.I epithelium and stroma, followed by a gradual decrease in STIC.C (4-fold) and cancer (2-fold), particularly in the epithelium (Fig. 6A and B).

Although the total number of CD8+ T cells decreased in later stages of HGSOC progression, the remaining CD8+ T cells were more likely to be either activated (PD1+ or Ki67+) or exhausted (LAG3+ or PD1+LAG3+), indicating a balance between active surveillance and T-cell dysfunction (Fig. 6C, D, and G–O; Supplementary Figs. S26A–S26N and S27A–S27D). Whereas 11% of CD8+ T cells in p53.I showed signs of activation, this fraction rose significantly in STIC.I, STIC.C, and cancer (25%–43%). Similarly, exhaustion markers increased in the epithelial compartments (Fig. 6C), with the proportion of exhausted CD8+ T cells rising 3- to 7-fold (~2% were LAG3+ T_{RM} CD8+ T cells in STIC.I, STIC.C, and cancer; 1% were LAG3+ CTL CD8+ T cells in STIC.C and cancer; Supplementary Fig. S26A). In the stroma of STIC.I, STIC.C, and cancer, ~1-2% of CD8+ T cells were LAG3+ T_{RM} and ~2% were LAG3+ CTL (Fig.6D; Supplementary Fig. S26B). The increased expression of RNA for *CTLA4* and *HAVCR2* (TIM3; Fig. 6P and Q) and GZMB protein and RNA (Supplementary Figs. S27E, S27F, S20E, and S20F) provided further evidence of activation and exhaustion in both the epithelium and stroma of HGSOC lesions (Supplementary Fig. S28). One contributing factor to this exhaustion may be chronic IFN signaling in later disease stages, as shown by a positive correlation between IRDS gene expression and T-cell exhaustion in the epithelium (Supplementary Fig. S29A–S29C). This suggests active immune surveillance by both T_{RM} and CTL, as well as conditions supporting immune editing and selection in HGSOC precursors.

DISCUSSION

We have developed a multi-patient and multistage resource of high-plex imaging and spatial transcriptomics data with which to study HGSOC development, from precancer lesions (p53.I signatures and STIC.Is) to invasive cancer. Our analysis reveals that localized IFN signaling and CIN are early events that increase with progression, accompanied by significant reorganization of the immune microenvironment. Activated T_{RM} and components of the NK–cDC1 axis are already present at the p53 signature stage, indicating early immune surveillance at the inception of HGSOC development in the FT. This immune response intensifies with increased abundance of activated CTLs in STIC.I lesions. However, during the

Figure 7. ***(Continued)*** into cancer. Early on, despite limited genomic instability, innate immune responses, including the NK–cDC1–CTL axis and T_{RM} cells, help contain p53 signature cells. Increasing aneuploidy or extrinsic factors can enhance immune surveillance, potentially eliminating precancer clones before significant proliferation occurs. During early STIC expansion, there is pronounced IFN response activation, with activated cDC1 and APCs and NK cell–secreted chemokines, further attracting cDC1. This environment suggests active immune surveillance and is accompanied by interactions among APCs, activated CD4+, and CD8+ T cells. However, immunosuppressive cells, such as M2-like macrophages and Tregs, also emerge, indicating a complex equilibrium in which cytotoxic and suppressive forces coexist. As STIC lesions advance, there is a reduction in CD8+ T cells and the interactions between APCs and CD4+ T cells, along with an increase in exhausted CD8+ CTL and CD4+ cells expressing LAG3, almost no NK and cDC1 cells, and more suppressive APCs. The transition from STIC to overt cancer involves hallmark mechanisms such as TGF-β signaling, which excludes CTLs, changes in cytokine and fibroblast profiles, and induction of EMT and migratory programs. Dotted arrows indicate the hypothetical timing of these events, suggesting a prolonged interval from p53 signature to early STIC, followed by a more rapid progression from early to late STIC. (Created with BioRender.com.)

transition from STIC.I to cancer-associated STIC, we observe a significant decrease in the NK–cDC1 axis. This decline coincides with an increase in activated $CD8^+$ T cells, exclusion and dysfunction of these cells, reduction of $CD4^+$ T cell–APC interactions, and increase in Tregs. These findings highlight a dynamic competition between immune surveillance and immune suppression, in which initial immune responses in early lesions are progressively antagonized by immune-suppressive mechanisms as HGSOC progresses (Fig. 7A and B).

The molecular heterogeneity observed in precancer lesions offers insights into interactions between the immune response and precursor phenotypes. Early localized IFN activation in p53 signatures and STICs, combined with the gradual accumulation of tumorigenic programs downstream of cGAS-STING or IFN pathways—such as NF-κB, IRDS, or IL6 induced STAT3 pathways (41, 74, 91)—may drive immune editing and selection in precursor populations. Traditionally, this heterogeneity and extensive genomic instability [including MN rupture and the catastrophic genomic events that drive genome evolution, immune evasion, and disease spread (41, 63, 64, 72)] have been viewed as hallmarks of later tumor evolution and chemoresistance (3, 14, 25, 56, 92). However, our data suggest that these processes are likely to be influential much earlier in HGSOC development. This phenotypic variability in STIC lesions, including differences in proliferation and DNA damage, may help inform diagnostic risk stratification by identifying STIC lesions with increased potential for malignant transformation and dissemination (93, 94). Variability in STIC microenvironment coupled with known genetic alterations in HGSOC, such as 6p loss leading to MHC class I loss and 6q loss affecting IFN-γ receptor 1 (*IFNGR1*; refs. 25, 56, 92, 95), highlights the potential for intricate interplay between genetic mutations, precursor cell phenotypes, and localized immune interactions during cancer development (96).

Immune evasion is a critical factor in HGSOC progression. Along the progression axis, IFN signaling coincides with HLA-A expression, responsible for antigen presentation to CTLs. However, upregulation of HLA-E expression may represent a key immune suppression mechanism during STIC clonal expansion. This aligns with findings in other cancers, in which high HLA-E expression inhibits NK cell activity by engaging NKG2A receptors, thereby suppressing NK cell–mediated cytotoxicity (46, 48, 60–62). The observed decline in the NK–cDC1 axis and dysfunction in adaptive immunity suggests that targeting NK cell reactivation using therapies such as humanized anti-NKG2A antibodies [e.g., monalizumab (60)] may be a promising strategy for early intervention, particularly in high-risk patients with STIC.I lesions linked to peritoneal cancer development (9). However, more detailed NK cell profiling will be needed to understand the functions of NK cells in HGSOC evolution.

Immune surveillance, driven by activated NK cells, cDC1, and T_{RM} cells, along with elevated *IFNG* and *TNF* (77, 89, 90) in the adjacent stroma, likely restrains the progression of early lesions, such as p53 signatures. This environment, sustained by feedback established between these immune cell types and recruited CTLs, may limit abnormal growth and prevent cancer progression. However, for clonal selection and expansion to occur, additional factors are likely required (97–99). These likely occur over the course of decades (7, 8, 10, 11, 13) and include repeated ovulatory-related stress leading to epithelial damage, increased cell proliferation, and genomic instability (8, 100). High STING expression in ciliated cells of the FT (55) may prime these cells to protect neighboring secretory cells from transformation arising from ovulatory-related stress and DNA damage, potentially suppressing the development and progression of precursor lesions. These ciliated cells are generally lost during the transition from p53 signatures to STIC, both within the precursors themselves and in the neighboring normal FT, eliminating their protective function. Within precursor lesions, a shift in the IFN response from early immune surveillance to chronic stimulation, may further promote IRDS and IFNε suppression (41); this serves to induce tolerance to DNA damage, immune suppression, and T-cell exhaustion. Furthermore, macrophage-derived APCs, although increasing in prevalence in later stages, show reduced interaction with $CD4^+$ T cells, indicating a functional shift that also promotes a transition from activation to immune suppression (80, 83). Thus, multiple coupled changes in epithelial cells and the TME are likely to play a role in the progression to more advanced stages of disease.

In summary, our findings suggest that failure of the NK–CTL axis combined with microenvironment remodeling that promotes immune evasion and CTL inhibition are critical drivers of early HGSOC development (101). Our data provide detailed insights into the temporal and spatial changes in the immune landscape and molecular transitions during HGSOC progression that are broadly consistent with an emerging view of precancer evolution. The data also serve as a large-scale public resource for further exploration of the interactions between transcriptional changes, cellular phenotypes, and immune organization in precancer ecosystems. To facilitate future studies on mechanisms driving cancer development and progression, we have integrated our spatial transcriptomics and imaging data into an enhanced version of cBioPortal. We expect that these studies will yield new strategies for prevention, diagnosis, and early intervention in HGSOC (102).

Limitation of the Study

Although this study provides insights into the immune landscape of HGSOC development and represents the largest available dataset of transcriptional and multiplexed imaging data of precancer, the sample size is still limited relative to the complexity of the disease and interpatient variability. Analysis of additional specimens will be needed to fully describe immune response across the HGSOC spectrum. In addition, 25% of STIC lesions associated with cancer have been reported to be disseminated cancer cells, reflecting the complexity of studying HGSOC progression in clinical settings (12). Expanding the cohort to include more STIC.I lesions would allow for the discovery of additional mechanisms relevant to disease progression and improve the identification of markers linked to clinical outcomes, offering a more complete understanding of HGSOC progression.

METHODS

Patient Specimens and Experimental Design

In total, 43 patients were identified from the University of Pennsylvania and the Swedish Cancer Institute, Seattle, hospital databases, which met our criteria of the presence of either STIC.I lesions ($n = 9$),

p53.I signatures ($n = 10$), or STIC with concurrent carcinoma ($n = 24$). After Institutional Review Board approval, serial sections of 5 µm thickness were processed. H&E stain was performed from the same block for CyCIF and GeoMx analyses (R. Drapkin, N. Shih, S. Coy) to confirm the diagnosis. One specimen per patient was processed, except one, patient 11 (bilateral STIC with concurrent carcinoma whereby both specimens were processed). In total, 44 formalin-fixed, paraffin-embedded specimens were collected, and all were processed for multiplex imaging using CyCIF. For microregion whole transcriptomics (GeoMx), 35/44 specimens were available and processed with more than 600 ROIs (n = initial 603 ROI collection), including normal FT/Fim, precancer lesions, and/or cancer. Tissue processing for both techniques is in Supplementary Methods.

2D CyCIF

Protocol for CyCIF was performed as described as Lin and colleagues (28, 54). The detailed protocol is available in protocols.io (https://doi.org/10.17504/protocols.io.bjiukkew). In brief, the slides were baked at 55°C to 60°C for 55 minutes prior to shipping. Then upon receiving the slides, BOND RX Automated IHC/ISH Stainer was used to bake formalin-fixed, paraffin-embedded slides at 60°C for 15 minutes, to dewax the sections using Bond Dewax solution at 72°C, and for antigen retrieval using Epitope Retrieval 1 (Leica) solution at 100°C for 20 minutes. Slides underwent multiple cycles of antibody incubation, imaging, and fluorophore inactivation. All antibodies were incubated overnight at 4°C in dark. Coverslips were wet-mounted using 200 µL of 50% glycerol/PBS before imaging. Images were acquired using a 20× objective (0.75 NA) on a CyteFinder slide scanning fluorescence microscope (RareCyte Inc.). Fluorophores were inactivated using a 4.5% H_2O_2, 24 mmol/L NaOH/PBS solution and an LED light source for 1 hour. The details of the antibody panel, including Research Resource Identifiers, used in this study are mentioned in Supplementary Table S4.

Image Processing and Quality Control

Image processing and analysis was performed with the Docker-based NextFlow pipeline MCMICRO (https://github.com/labsyspharm/mcmicro; ref. 32) and with customized scripts in MATLAB (version R2024a; MathWorks Inc.: https://www.mathworks.com/products/matlab.html; ref. 54) and R (version 4.3.3) as described previously. Briefly, raw images were stitched and registered from the different tiles and cycles after the acquisition using the ASHLAR (103) module within the MCMICRO pipeline. After the registration step, the OME.TIFF files from each slide were passed through the quantification module of MCMICRO. Overall, UNMICST2 (104) was used for segmentation and quantification to generate single-cell data. Quality control (QC) of the single-cell data includes removing cycles in which tissue loss was observed, as previously published, to have the final single-cell feature table (54).

Cell Type Identification

All samples and markers were gated independently using an open-source "gator" viewing and analysis tool as well as binary gating as described previously (54). The details of gator can be found at https://github.com/labsyspharm/minerva_analysis/wiki/Gating. After generating the initial gate, visual inspection and adjustment was made to the final gating table to incorporate with single-cell feature table. For cell type and state identification, preexisting knowledge based on literature was used as described (54).

Cell Population Proportions

After calculating the average proportion of cells expressing single/double/triple markers for cell phenotyping on MATLAB, downstream quantification across HGSOC stages, including statistical analysis, was performed in R (version 4.3.3). To test whether proportions of cells with a given phenotype among the whole populations of cells differed between disease stages, we used binomial generalized linear mixed models (LMMs implemented in the lme4 R package (version 1.1-34; Bates and colleagues 2014: http://arxiv.org/abs/1406.5823). For each ROI, the number of cells with the given phenotype ("successes") and of all other phenotypes ("failures") were modeled using the binomial distribution with a logit link function using the lme4 model formula cbind(n_success, n_failure) ~ stage + (1 + stage|patient_id). ROIs were not independent because they were derived from the same patients more than once. To account for this, covariance and patient-specific effects were modeled by including random intercepts and stage coefficients for each patient. Post hoc contrasts between stages were performed using the emmeans R package with Benjamini–Hochberg correction for multiple testing. Due to the overdispersion of some immune populations, we used binomial generalized LMMs implemented in the glmmTMB R package (version 1.1.9; ref. 105) for six major subtypes of immune populations. For each ROI, the number of cells with the given phenotype ("successes") and of all other phenotypes ("failures") were modeled using the binomial distribution with a logit link function using the glmmTMB model formula cbind(n_success, n_failure) ~ stage + (1|patient_id) + (1|observation_id). ROIs were not independent because they were derived from the same patients more than once. To account for this, covariance and patient-specific effects were modeled by including random intercepts and stage coefficients for each patient. Overdispersion was controlled for by including an observation-level random effect (106). This model specification minimized the Akaike information criterion compared with other alternative specifications, including negative binomial, beta-binomial, and binomial models without observation-level random effect. We also tested adding the age of the patient as a variable. However, the model did not improve further. The data summary and statistics for all CyCIF analysis are in Supplementary Tables S5 and S6.

Neighborhood Analysis (LDA) and Cell–Cell Interactions

LDA analysis for spatial topic analysis was performed using MATLAB *fitlda* function as described previously (54). The pooled frequencies of all samples were used to train the final LDA model, and 21 topics were isolated. To inspect cell–cell interactions, especially between two types of immune cells, a cell type–dependent interaction score was generated (107) by a custom MATLAB script, whereby >1 indicates a close proximity between two cell types and *vice versa*. The score was normalized against the distance of random sampling of two cell types of interest and then compared with different stages of HGSOC progression. To allow for the permutation step, only samples with both cell types >5 cells were included with further manual inspection of each cell type/sample for each stage of HGSOC progression. The interaction score was normalized against the distance of random sampling. Because at least five cells of both populations will have to be present for random sampling, the number of specimens analyzed from tissue imaging was STIC.I ($n = 7$), STIC.C ($n = 16$; $P = 0.03$; cDC1 and activated $CD4^+$); STIC.I ($n = 7$), STIC.C ($n = 12$; $P = 0.02$; HLA-DR^+ $CD68^+$ APCs and activated $CD4^+$); and STIC.I ($n = 7$), STIC.C ($n = 14$; $P = 0.04$; HLA-DR^+CD68^+ and activated $CD8^+$). The details of cell types and size comparing STIC.I versus STIC.C is in Supplementary Table S5.

3D CyCIF and Image Processing

One of the cases of STIC coexisting with cancer was processed (20 µm thickness) for super high-resolution imaging as detailed in Yapp C and colleagues (bioRxiv 2024; https://www.biorxiv.org/content/10.1101/2023.11.10.566670v4) using a Zeiss LSM980 confocal microscope (Supplementary Method). The staining protocol is similar to standard 2D CyCIF with overnight antibody incubation. The details of the antibody panel, including Research Resource Identifiers, are mentioned in Supplementary Table S4.

Annotation, Selection of ROIs, and Protocol for Microregion Spatial Transcriptomics

For microregion spatial transcriptomic profiling, we have used the GeoMx platform with the whole transcriptome (WTA) probe sets (NanoString) as previously published (75). The ROIs were annotated by a board-certified pathologist (S. Coy) based on H&E and visualizing images from CyCIF (Cycle 1–6). Because we wanted to integrate RNA and protein expression, we have annotated all ROIs based on the presence or absence of *HLA-E* expression in both epithelium and epithelium–stroma boundary (i.e., adjacent stroma). Unlike the cancer group, adjacent stromal compartments of normal FT or Fim were collected for all incidental cases when available (Supplementary Fig. S2). NanoString GeoMx gene expression analysis utilizing the whole transcriptome (WTA) probe set was performed using previously described methods (75). The WTA probe set is in Supplementary Table S7, keeping in mind that few probes were generic, meaning NanoString could not design those probes for specific receptors, such as *KLRC2* and *KLRC1*, such that both receptors are displayed by "*KLRC2*." Briefly, a 5-μm section was dewaxed and stained overnight with antibodies targeting epithelial (pan-cytokeratin) and immune cells (CD45), defining cell morphology and highlighting ROIs. The section was hybridized with the WTA probes before being loaded into the instrument. In total, 603 ROIs were initially selected for collection and library preparation. Followed by QC, 542 ROIs representing different stages of the disease progression were used for downstream analysis in this study (Supplementary Methods).

Data Processing and QC for GeoMx Data

All sample processing and sequencing were performed by the Dana Farber Institute or Harvard Medical School facility. The QC and the quartile-3 (Q3) normalization of the initial data set were performed as suggested by NanoString using GeoMx DSP software, NanoString (version 3.1.0.221). The detailed steps of QCs are mentioned in Supplementary Methods. The annotation of these ROIs after the QC is detailed in Supplementary Table S2. The ROI numbers for each lesion type are depicted in Supplementary Fig. S2. The Q3-normalized count matrix file after the QC and segment and probe properties are in Supplementary Tables S8 and Table S9, respectively.

Spatial Integration of CyCIF and GeoMx Data

To establish the mapping between GeoMx ROIs and CyCIF data, the DNA channel in both whole-slide images was used. The process begins by deriving a global affine transformation between the downsized whole-slide images of the GeoMx and CyCIF datasets. In the second step, we query 2D image patches at full resolution, centered around the ROI centroids in the GeoMx image and their corresponding locations in the CyCIF image, based on the global affine transformation. These pairs of image patches are then used for a second round of affine registration. Both rounds of affine registration are conducted using Oriented FAST and Rotated BRIEF (108) feature detection and matching techniques. We processed the quantification from integrated ROIs from GeoMx, similar to 2D CyCIF as described earlier.

Differential Gene Expression and GSEA

To identify sets of genes that were highly or lowly expressed, differential gene expression was performed using GeoMx DSP software, NanoString (version 3.1.0.221), using the Q3-normalized counts. DSP software was used for LMMs with Benjamini–Hochberg correction to perform differential gene expression. Model formula: lesion type + (1|scan_ID) whereby scan_ID refers to the patient/slide ID. The LMM is designed to handle data with repeated measurements from the same sampling unit, and scan_ID was chosen as a random effect. DSP software's custom R script provided by NanoString was used to visualize the data for differential gene expression as a volcano plot.

The output of differentially expressed genes was exported from the DSP software [i.e., a ranked list of differentially expressed genes between two sets of experimental conditions, such as p53.I (epithelial) versus STIC.I (epithelial), shown in Fig. 2A and B]. Then GSEA analysis using MsigDB (35) Cancer Hallmark pathways and reactome pathways (36) were performed. MsigDB GSEA was performed in R (version 4.3.3) using msigdbr (hallmark gene set, category = = H) and fgsea packages. GSEA on reactome database was performed using GeoMx DSP software and visualized using R. The output for reactome pathways shown in Supplementary Fig. S4A and S4B is also provided in Supplementary Tables S10 and S11. The visualization of the GSEA was adapted (109).

Modeling the Progression of HGSOC Using Published Gene Set by Bayesian Regression Modeling

To study the relationship between gene expression and cancer lesion progression, we used a Bayesian ordinal regression model implemented by the brms R package (110). We preprocessed GeoMx expression counts by Q3 normalized to account for sequencing depth, followed by $\log_{10}$ transformation to stabilize variances. To account for differences in expression levels across genes, we further normalized the log-transformed values by scaling to a mean of zero and variance of one (z-transform). We fitted one model per gene using the model specification gene_expression ~ mo(stage) + [1 + mo(stage)|patient_id] (Fig. 2E and F; Supplementary Fig. S14A–S14G). The lesion stage was used as ordinal predictor mo(stage) with a monotonic constraint to enforce the assumption of an orderly sequence of stages. We accounted for repeat measurements from the same patients by including patient-specific random intercepts and stage coefficients. To model expression of gene sets, we modified the model to include another random effect and its interaction with patient_id (gene_expression ~ mo(stage) + [1 + mo(stage)|patient_id * gene]. This modification allows every patient and gene to have a different expression baseline and expression changes at each disease stage. The "*" operator between patient and gene enables genes to behave differently in every patient (i.e., interaction). As a result, we can look at the expression along with the progression axis as a gene set, such as the IRDS gene set shown in Supplementary Fig. S14E. To investigate the effect of HLA-E expression on other genes, we further modified the model to include a fixed effect coefficient serving as binary indicator for presence or absence of HLA-E in the CyCIF image of the ROI (gene_expression ~ mo(stage) * hlae_e + [1 + mo(stage) * hlae_e|patient_id * gene]. We tested this modified model first to confirm whether HLA-E expression in protein and RNA levels match. Supplementary Figure S14C indicates that *HLA-E* RNA expression is higher in clones that are HLA-E$^+$ by CyCIF, including an increased trend observed from FT.C to cancer. For significance testing, we used the proportion of the 95% highest density interval within the region of practical equivalence (0.05 times the SD). Comparisons with >95% of the highest density interval outside the region of practical equivalence were significant (*), whereas those with >99% were considered very significant (**; ref. 111). In most cases, matched FT was chosen as a reference, meaning p53.I and STIC.I were compared with FT.I, and STIC.C and cancer were compared with FT.C. One exception was the stromal component from the cancer group, in which we used p53.C as a reference due to the unavailability of normal FT or Fim from this group.

Statistical Analysis

All statistical significance is considered $P < 0.05$ unless stated otherwise. Other statistical analyses, such as *t* test, were performed using R (version 4.3.3) or Graph Pad Prism [version 10.0.2 (232)].

Data Availability

Both CyCIF images and GeoMx data are available through https://www.cbioportal.org/study/summary?id=ovary_geomx_gray_foundation_2024. GeoMx data are available as Count Matrix as a Supplementary Table S8 through https://doi.org/10.5281/zenodo.14502077. Raw files for GeoMx are submitted to Gene Expression Omnibus (Accession number: GSE281193). New codes for this manuscript are available at https://github.com/labsyspharm/stic-ms-2024. More information about the dataset will be found at https://www.graybrcaatlas.org/atlas-datasets/kader-lin-hug-2024/. The data is available at the HTAN Data Portal (https://data.humantumoratlas.org/). See Supplementary Table S1 for the HTAN IDs of each sample.

Authors' Disclosures

Y.-A. Chen is a consultant for RareCyte. J.R. Heath reports grants from the NCI, Andy Hill Care Fund, and the Paul Allen Foundation during the conduct of the study, as well as nonfinancial support from AtlasXomics outside the submitted work. C.W. Drescher reports grants from the Gray Foundation and Canary Foundation during the conduct of the study. P.K. Sorger reports grants and personal fees from RareCyte Inc., personal fees from Glencoe Inc., and personal fees from NanoString/Bruker during the conduct of the study, as well as personal fees from Merck and Montai Inc. outside the submitted work. R. Drapkin reports personal fees from Repare Therapeutics outside the submitted work. S. Santagata reports personal fees from Roche and Novartis and grants from Merck outside the submitted work. No disclosures were reported by the other authors.

Authors' Contributions

T. Kader: Conceptualization, data curation, formal analysis, investigation, visualization, methodology, writing–original draft, writing–review and editing. **J.-R. Lin:** Conceptualization, data curation, software, formal analysis, investigation, visualization, methodology, writing–review and editing. **C.B. Hug:** Data curation, formal analysis, investigation, methodology, writing–review and editing. **S. Coy:** Investigation, visualization, methodology. **Y.-A. Chen:** Data curation, software, formal analysis, investigation, visualization, methodology, writing–review and editing. **I. de Bruijn:** Data curation, software, visualization, methodology, cBioPortal team. **N. Shih:** Resources, investigation, visualization. **E. Jung:** Resources, investigation. **R.J. Pelletier:** Formal analysis, investigation, methodology. **M. Lopez Leon:** Formal analysis, investigation, visualization. **G. Mingo:** Investigation. **D.K. Omran:** Resources, investigation. **J.S. Lee:** Formal analysis, investigation, visualization. **C. Yapp:** Software, formal analysis, investigation, visualization, methodology. **B.A. Satravada:** Data curation, software, visualization, cBioPortal team. **R. Kundra:** Data curation, software, visualization, cBioPortal team. **Y. Xu:** Formal analysis, investigation, visualization, writing–review and editing. **S. Chan:** Investigation. **J.B. Tefft:** Visualization, writing–review and editing. **J.L. Muhlich:** Data curation, software, formal analysis, investigation, visualization, methodology. **S.H. Kim:** Resources. **S.M. Gysler:** Resources. **J. Agudo:** Investigation, writing–review and editing. **J.R. Heath:** Resources. **N. Schultz:** Software, visualization, methodology. **C.W. Drescher:** Resources, writing–review and editing. **P.K. Sorger:** Conceptualization, resources, software, supervision, funding acquisition, investigation, visualization, methodology, project administration, writing–review and editing. **R. Drapkin:** Conceptualization, resources, supervision, funding acquisition, investigation, methodology, project administration, writing–review and editing. **S. Santagata:** Conceptualization, resources, software, supervision, funding acquisition, validation, investigation, visualization, methodology, project administration, writing–review and editing.

Acknowledgments

We thank the MicRoN core facility at Harvard Medical School for providing access to an LSM980 Airyscan 2 microscope. We would like to acknowledge the use of ChatGPT 4.0 for suggesting text edits to enhance clarity, assisting in revising existing text written by the authors. This study was funded by the Gray Foundation (P.K. Sorger, C.W. Drescher, R. Drapkin, and S. Santagata), Ludwig Cancer Research (P.K. Sorger and S. Santagata), the Canary Foundation (C.W. Drescher and R. Drapkin), NCI grants U2C-CA233262 (P.K. Sorger and S. Santagata), U54-CA268072 (P.K. Sorger, C. Yapp), U01-CA284207 (S. Santagata) and P50-CA228991 (R. Drapkin), the Department of Defense W81XWH-22-1-0852 (R. Drapkin), the Dr. Miriam and Sheldon G. Adelson Medical Research Foundation (R. Drapkin), the Honorable Tina Brozman Foundation for Ovarian Cancer Research (R. Drapkin), the Mike and Patti Hennessy Foundation (R. Drapkin), and the Carl H. Goldsmith Ovarian Cancer Translational Research Fund (R. Drapkin). This work was also supported by the Bridge Project between the Koch Institute at MIT and DF/HCC. S. Coy is supported by funding from the Program for Interdisciplinary Neuroscience at Harvard Medical School. J.-R. Lin is supported by R50 (R50-CA274277). S. Santagata is supported by the BWH President's Scholars Award.

Note

Supplementary data for this article are available at Cancer Discovery Online (http://cancerdiscovery.aacrjournals.org/).

Received September 23, 2024; revised November 15, 2024; accepted December 17, 2024; posted first December 20, 2024.

REFERENCES

1. Bray F, Laversanne M, Sung H, Ferlay J, Siegel RL, Soerjomataram I, et al. Global cancer statistics 2022: GLOBOCAN estimates of incidence and mortality worldwide for 36 cancers in 185 countries. CA Cancer J Clin 2024;74:229–63.
2. Kroeger PT Jr, Drapkin R. Pathogenesis and heterogeneity of ovarian cancer. Curr Opin Obstet Gynecol 2017;29:26–34.
3. Bowtell DD, Böhm S, Ahmed AA, Aspuria P-J, Bast RC Jr, Beral V, et al. Rethinking ovarian cancer II: reducing mortality from high-grade serous ovarian cancer. Nat Rev Cancer 2015;15:668–79.
4. Lee Y, Miron A, Drapkin R, Nucci MR, Medeiros F, Saleemuddin A, et al. A candidate precursor to serous carcinoma that originates in the distal fallopian tube. J Pathol 2007;211:26–35.
5. Medeiros F, Muto MG, Lee Y, Elvin JA, Callahan MJ, Feltmate C, et al. The tubal fimbria is a preferred site for early adenocarcinoma in women with familial ovarian cancer syndrome. Am J Surg Pathol 2006;30:230–6.
6. Kindelberger DW, Lee Y, Miron A, Hirsch MS, Feltmate C, Medeiros F, et al. Intraepithelial carcinoma of the fimbria and pelvic serous carcinoma: evidence for a causal relationship. Am J Surg Pathol 2007;31:161–9.
7. Fathalla MF. Incessant ovulation and ovarian cancer - a hypothesis re-visited. Facts Views Vis Obgyn 2013;5:292–7.
8. Emori MM, Drapkin R. The hormonal composition of follicular fluid and its implications for ovarian cancer pathogenesis. Reprod Biol Endocrinol 2014;12:60.
9. Steenbeek MP, Van Bommel MH, Bulten J, Hulsmann JA, Bogaerts J, Garcia C, et al. Risk of peritoneal carcinomatosis after risk-reducing salpingo-oophorectomy: a systematic review and individual patient data meta-analysis. J Clin Oncol 2022;40:1879–91.
10. Soong TR, Howitt BE, Horowitz N, Nucci MR, Crum CP. The fallopian tube,"precursor escape" and narrowing the knowledge gap to the origins of high-grade serous carcinoma. Gynecol Oncol 2019;152:426–33.
11. Wu R, Wang P, Lin S, Zhang M, Song Q, Chu T, et al. Genomic landscape and evolutionary trajectories of ovarian cancer precursor lesions. J Pathol 2019;248:41–50.

12. Eckert MA, Pan S, Hernandez KM, Loth RM, Andrade J, Volchenboum SL, et al. Genomics of ovarian cancer progression reveals diverse metastatic trajectories including intraepithelial metastasis to the fallopian tube. Cancer Discov 2016;6:1342–51.
13. Labidi-Galy SI, Papp E, Hallberg D, Niknafs N, Adleff V, Noe M, et al. High grade serous ovarian carcinomas originate in the fallopian tube. Nat Commun 2017;8:1093.
14. Wang YK, Bashashati A, Anglesio MS, Cochrane DR, Grewal DS, Ha G, et al. Genomic consequences of aberrant DNA repair mechanisms stratify ovarian cancer histotypes. Nat Genet 2017;49:856–65.
15. Pisanic TR, Cope LM, Lin SF, Yen T-T, Athamanolap P, Asaka R, et al. Methylomic analysis of ovarian cancers identifies tumor-specific alterations readily detectable in early precursor lesions. Clin Cancer Res 2018;24:6536–47.
16. Pisanic TR, Wang Y, Sun H, Considine M, Li L, Wang TH, et al. Methylomic landscapes of ovarian cancer precursor lesions. Clin Cancer Res 2020;26:6310–20.
17. Klinkebiel D, Zhang W, Akers SN, Odunsi K, Karpf AR. DNA methylome analyses implicate fallopian tube epithelia as the origin for high-grade serous ovarian cancer. Mol Cancer Res 2016;14:787–94.
18. Brown VE, Moore SL, Chen M, House N, Ramsden P, Wu HJ, et al. CDK2 regulates collapsed replication fork repair in CCNE1-amplified ovarian cancer cells via homologous recombination. NAR Cancer 2023;5:zcad039.
19. Karst AM, Jones PM, Vena N, Ligon AH, Liu JF, Hirsch MS, et al. Cyclin E1 deregulation occurs early in secretory cell transformation to promote formation of fallopian tube–derived high-grade serous ovarian cancers. Cancer Res 2014;74:1141–52.
20. Kuhn E, Wang TL, Doberstein K, Bahadirli-Talbott A, Ayhan A, Sehdev AS, et al. CCNE1 amplification and centrosome number abnormality in serous tubal intraepithelial carcinoma: further evidence supporting its role as a precursor of ovarian high-grade serous carcinoma. Mod Pathol 2016;29:1254–61.
21. Cheng Z, Ennis DP, Lu B, Mirza HB, Sokota C, Kaur B, et al. The genomic trajectory of ovarian high-grade serous carcinoma can be observed in STIC lesions. J Pathol 2024;264:42–54.
22. Tothill RW, Tinker AV, George J, Brown R, Fox SB, Lade S, et al. Novel molecular subtypes of serous and endometrioid ovarian cancer linked to clinical outcome. Clin Cancer Res 2008;14:5198–208.
23. Hollis RL, Meynert AM, Michie CO, Rye T, Churchman M, Hallas-Potts A, et al. Multiomic characterization of high-grade serous ovarian carcinoma enables high-resolution patient stratification. Clin Cancer Res 2022;28:3546–56.
24. Kandalaft LE, Dangaj Laniti D, Coukos G. Immunobiology of high-grade serous ovarian cancer: lessons for clinical translation. Nat Rev Cancer 2022;22:640–56.
25. Vázquez-García I, Uhlitz F, Ceglia N, Lim JLP, Wu M, Mohibullah N, et al. Ovarian cancer mutational processes drive site-specific immune evasion. Nature 2022;612:778–86.
26. Lee SK, Kim CJ, Kim DJ, Kang JH. Immune cells in the female reproductive tract. Immune Netw 2015;15:16–26.
27. Ardighieri L, Lonardi S, Moratto D, Facchetti F, Shih I-M, Vermi W, et al. Characterization of the immune cell repertoire in the normal fallopian tube. Int J Gynecol Pathol 2014;33:581–91.
28. Lin J-R, Izar B, Wang S, Yapp C, Mei S, Shah PM, et al. Highly multiplexed immunofluorescence imaging of human tissues and tumors using t-CyCIF and conventional optical microscopes. Elife 2018;7:e31657.
29. Baysoy A, Bai Z, Satija R, Fan R. The technological landscape and applications of single-cell multi-omics. Nat Rev Mol Cell Biol 2023;24:695–713.
30. Ben-David U, Amon A. Context is everything: aneuploidy in cancer. Nat Rev Genet 2020;21:44–62.
31. Nowell PC. The clonal evolution of tumor cell populations. Science 1976;194:23–8.
32. Schapiro D, Sokolov A, Yapp C, Chen YA, Muhlich JL, Hess J, et al. MCMICRO: a scalable, modular image-processing pipeline for multiplexed tissue imaging. Nat Methods 2022;19:311–5.
33. Cancer Genome Atlas Research Network. Integrated genomic analyses of ovarian carcinoma. Nature 2011;474:609–15.
34. Ahmed AA, Etemadmoghadam D, Temple J, Lynch AG, Riad M, Sharma R, et al. Driver mutations in TP53 are ubiquitous in high grade serous carcinoma of the ovary. J Pathol 2010;221:49–56.
35. Liberzon A, Birger C, Thorvaldsdóttir H, Ghandi M, Mesirov JP, Tamayo P. The Molecular Signatures Database (MSigDB) hallmark gene set collection. Cell Syst 2015;1:417–25.
36. Fabregat A, Jupe S, Matthews L, Sidiropoulos K, Gillespie M, Garapati P, et al. The reactome pathway knowledgebase. Nucleic Acids Res 2018;46:D649–55.
37. Tyler M, Tirosh I. Decoupling epithelial-mesenchymal transitions from stromal profiles by integrative expression analysis. Nat Commun 2021;12:2592.
38. Szabo PM, Vajdi A, Kumar N, Tolstorukov MY, Chen BJ, Edwards R, et al. Cancer-associated fibroblasts are the main contributors to epithelial-to-mesenchymal signatures in the tumor microenvironment. Sci Rep 2023;13:3051.
39. Massagué J, Sheppard D. TGF-β signaling in health and disease. Cell 2023;186:4007–37.
40. Weichselbaum RR, Ishwaran H, Yoon T, Nuyten DSA, Baker SW, Khodarev N, et al. An interferon-related gene signature for DNA damage resistance is a predictive marker for chemotherapy and radiation for breast cancer. Proc Natl Acad Sci U S A 2008;105:18490–5.
41. Cheon H, Wang Y, Wightman SM, Jackson MW, Stark GR. How cancer cells make and respond to interferon-I. Trends Cancer 2023;9:83–92.
42. Marks ZRC, Campbell NK, Mangan NE, Vandenberg CJ, Gearing LJ, Matthews AY, et al. Interferon-ε is a tumour suppressor and restricts ovarian cancer. Nature 2023;620:1063–70.
43. Mayall JR, Horvat JC, Mangan NE, Chevalier A, McCarthy H, Hampsey D, et al. Interferon-epsilon is a novel regulator of NK cell responses in the uterus. EMBO Mol Med 2024;16:267–93.
44. Bürkner P-C, Charpentier E. Modelling monotonic effects of ordinal predictors in Bayesian regression models. Br J Math Stat Psychol 2020;73:420–51.
45. Borrego F, Ulbrecht M, Weiss EH, Coligan JE, Brooks AG. Recognition of human histocompatibility leukocyte antigen (HLA)-E complexed with HLA class I signal sequence–derived peptides by CD94/NKG2 confers protection from natural killer cell–mediated lysis. J Exp Med 1998;187:813–8.
46. Borst L, van der Burg SH, van Hall T. The NKG2A-HLA-E axis as a novel checkpoint in the tumor microenvironment. Clin Cancer Res 2020;26:5549–56.
47. Levy EM, Bianchini M, Von Euw EM, Barrio MM, Bravo AI, Furman D, et al. Human leukocyte antigen-E protein is overexpressed in primary human colorectal cancer. Int J Oncol 2008;32:633–41.
48. Seliger B, Jasinski-Bergner S, Quandt D, Stoehr C, Bukur J, Wach S, et al. HLA-E expression and its clinical relevance in human renal cell carcinoma. Oncotarget 2016;7:67360–72.
49. Zheng H, Guan X, Meng X, Tong Y, Wang Y, Xie S, et al. IFNγ in ovarian tumor microenvironment upregulates HLA-E expression and predicts a poor prognosis. J Ovarian Res 2023;16:229.
50. Vijayan S, Sidiq T, Yousuf S, van den Elsen PJ, Kobayashi KS. Class I transactivator, NLRC5: a central player in the MHC class I pathway and cancer immune surveillance. Immunogenetics 2019;71:273–82.
51. Platanias LC. Mechanisms of type-I- and type-II-interferon-mediated signalling. Nat Rev Immunol 2005;5:375–86.
52. Fung KY, Mangan NE, Cumming H, Horvat JC, Mayall JR, Stifter SA, et al. Interferon-ε protects the female reproductive tract from viral and bacterial infection. Science 2013;339:1088–92.
53. Khodarev NN, Beckett M, Labay E, Darga T, Roizman B, Weichselbaum RR. STAT1 is overexpressed in tumors selected for radioresistance and confers protection from radiation in transduced sensitive cells. Proc Natl Acad Sci U S A 2004;101:1714–9.
54. Lin JR, Wang S, Coy S, Chen YA, Yapp C, Tyler M, et al. Multiplexed 3D atlas of state transitions and immune interaction in colorectal cancer. Cell 2023;186:363–81.e19.
55. Huvila J, Cochrane DR, Ta M, Chow C, Greening K, Leung S, et al. STING pathway expression in low-grade serous carcinoma of the

ovary: an unexpected therapeutic opportunity? J Pathol Clin Res 2021;7:548–55.
56. Burdett NL, Willis MO, Alsop K, Hunt AL, Pandey A, Hamilton PT, et al. Multiomic analysis of homologous recombination-deficient end-stage high-grade serous ovarian cancer. Nat Genet 2023;55:437–50.
57. Jamal-Hanjani M, Wilson GA, McGranahan N, Birkbak NJ, Watkins TBK, Veeriah S, et al. Tracking the evolution of non-small-cell lung cancer. N Engl J Med 2017;376:2109–21.
58. Huntington ND, Cursons J, Rautela J. The cancer–natural killer cell immunity cycle. Nat Rev Cancer 2020;20:437–54.
59. Fisher JG, Doyle ADP, Graham LV, Khakoo SI, Blunt MD. Disruption of the NKG2A:HLA-E immune checkpoint axis to enhance NK cell activation against cancer. Vaccines 2022;10:1993.
60. André P, Denis C, Soulas C, Bourbon-Caillet C, Lopez J, Arnoux T, et al. Anti-NKG2A mAb is a checkpoint inhibitor that promotes anti-tumor immunity by unleashing both T and NK cells. Cell 2018;175:1731–43.e13.
61. Liu X, Song J, Zhang H, Liu X, Zuo F, Zhao Y, et al. Immune checkpoint HLA-E:CD94-NKG2A mediates evasion of circulating tumor cells from NK cell surveillance. Cancer Cell 2023;41:272–87.e9.
62. Salomé B, Sfakianos JP, Ranti D, Daza J, Bieber C, Charap A, et al. NKG2A and HLA-E define an alternative immune checkpoint axis in bladder cancer. Cancer Cell 2022;40:1027–43.e9.
63. Zhang C-Z, Spektor A, Cornils H, Francis JM, Jackson EK, Liu S, et al. Chromothripsis from DNA damage in micronuclei. Nature 2015;522:179–84.
64. Mackenzie KJ, Carroll P, Martin C-A, Murina O, Fluteau A, Simpson DJ, et al. cGAS surveillance of micronuclei links genome instability to innate immunity. Nature 2017;548:461–5.
65. Tang Z, Yang J, Wang X, Zeng M, Wang J, Wang A, et al. Active DNA end processing in micronuclei of ovarian cancer cells. BMC Cancer 2018;18:426.
66. Sato S, Gillette M, de Santiago PR, Kuhn E, Burgess M, Doucette K, et al. LINE-1 ORF1p as a candidate biomarker in high grade serous ovarian carcinoma. Sci Rep 2023;13:1537.
67. Pisanic TR, Asaka S, Lin SF, Yen TT, Sun H, Bahadirli-Talbott A, et al. Long interspersed nuclear element 1 retrotransposons become deregulated during the development of ovarian cancer precursor lesions. Am J Pathol 2019;189:513–20.
68. De Cecco M, Ito T, Petrashen AP, Elias AE, Skvir NJ, Criscione SW, et al. L1 drives IFN in senescent cells and promotes age-associated inflammation. Nature 2019;566:73–8.
69. Xia Z, Cochrane DR, Tessier-Cloutier B, Leung S, Karnezis AN, Cheng AS, et al. Expression of L1 retrotransposon open reading frame protein 1 in gynecologic cancers. Hum Pathol 2019;92:39–47.
70. Macintyre G, Goranova TE, De Silva D, Ennis D, Piskorz AM, Eldridge M, et al. Copy number signatures and mutational processes in ovarian carcinoma. Nat Genet 2018;50:1262–70.
71. Hong C, Schubert M, Tijhuis AE, Requesens M, Roorda M, van den Brink A, et al. cGAS–STING drives the IL-6-dependent survival of chromosomally instable cancers. Nature 2022;607:366–73.
72. Bakhoum SF, Ngo B, Laughney AM, Cavallo JA, Murphy CJ, Ly P, et al. Chromosomal instability drives metastasis through a cytosolic DNA response. Nature 2018;553:467–72.
73. Singh S, Vaughan CA, Frum RA, Grossman SR, Deb S, Palit Deb S. Mutant p53 establishes targetable tumor dependency by promoting unscheduled replication. J Clin Invest 2017;127:1839–55.
74. Dhanisha SS, Guruvayoorappan C. Potential role of cGAS/STING pathway in regulating cancer progression. Crit Rev Oncol Hematol 2022;178:103780.
75. Nirmal AJ, Maliga Z, Vallius T, Quattrochi B, Chen AA, Jacobson CA, et al. The spatial landscape of progression and immunoediting in primary melanoma at single-cell resolution. Cancer Discov 2022;12:1518–41.
76. Lin JR, Chen YA, Campton D, Cooper J, Coy S, Yapp C, et al. High-plex immunofluorescence imaging and traditional histology of the same tissue section for discovering image-based biomarkers. Nat Cancer 2023;4:1036–52.
77. Böttcher JP, Reis e Sousa C. The role of type 1 conventional dendritic cells in cancer immunity. Trends Cancer 2018;4:784–92.
78. Böttcher JP, Bonavita E, Chakravarty P, Blees H, Cabeza-Cabrerizo M, Sammicheli S, et al. NK cells stimulate recruitment of cDC1 into the tumor microenvironment promoting cancer immune control. Cell 2018;172:1022–37.e14.
79. Laoui D, Keirsse J, Morias Y, Van Overmeire E, Geeraerts X, Elkrim Y, et al. The tumour microenvironment harbours ontogenically distinct dendritic cell populations with opposing effects on tumour immunity. Nat Commun 2016;7:13720.
80. Heras-Murillo I, Adán-Barrientos I, Galán M, Wculek SK, Sancho D. Dendritic cells as orchestrators of anticancer immunity and immunotherapy. Nat Rev Clin Oncol 2024;21:257–77.
81. Barry KC, Hsu J, Broz ML, Cueto FJ, Binnewies M, Combes AJ, et al. A natural killer–dendritic cell axis defines checkpoint therapy–responsive tumor microenvironments. Nat Med 2018;24:1178–91.
82. Mempel TR, Lill JK, Altenburger LM. How chemokines organize the tumour microenvironment. Nat Rev Cancer 2024;24:28–50.
83. Surówka J, Wertel I, Okła K, Bednarek W, Tarkowski R, Kotarski J. Influence of ovarian cancer type I and type II microenvironment on the phenotype and function of monocyte-derived dendritic cells. Clin Transl Oncol 2017;19:1489–97.
84. Qian J, Olbrecht S, Boeckx B, Vos H, Laoui D, Etlioglu E, et al. A pan-cancer blueprint of the heterogeneous tumor microenvironment revealed by single-cell profiling. Cell Res 2020;30:745–62.
85. de Mingo Pulido Á, Gardner A, Hiebler S, Soliman H, Rugo HS, Krummel MF, et al. TIM-3 regulates CD103^{+} dendritic cell function and response to chemotherapy in breast cancer. Cancer Cell 2018;33:60–74.e6.
86. de Mingo Pulido Á, Hänggi K, Celias DP, Gardner A, Li J, Batista-Bittencourt B, et al. The inhibitory receptor TIM-3 limits activation of the cGAS-STING pathway in intra-tumoral dendritic cells by suppressing extracellular DNA uptake. Immunity 2021;54:1154–67.e7.
87. Hu X-H, Tang M-X, Mor G, Liao A-H. Tim-3: expression on immune cells and roles at the maternal-fetal interface. J Reprod Immunol 2016;118:92–9.
88. Chiba S, Baghdadi M, Akiba H, Yoshiyama H, Kinoshita I, Dosaka-Akita H, et al. Tumor-infiltrating DCs suppress nucleic acid–mediated innate immune responses through interactions between the receptor TIM-3 and the alarmin HMGB1. Nat Immunol 2012;13:832–42.
89. Park SL, Gebhardt T, Mackay LK. Tissue-resident memory T cells in cancer immunosurveillance. Trends Immunol 2019;40:735–47.
90. Mueller SN, Mackay LK. Tissue-resident memory T cells: local specialists in immune defence. Nat Rev Immunol 2016;16:79–89.
91. Wang Y, Shen Y, Wang S, Shen Q, Zhou X. The role of STAT3 in leading the crosstalk between human cancers and the immune system. Cancer Lett 2018;415:117–28.
92. Burdett NL, Willis MO, Pandey A, Twomey L, Alaei S; Australian Ovarian Cancer Study Group; Bowtell DDL, et al. Timing of whole genome duplication is associated with tumor-specific MHC-II depletion in serous ovarian cancer. Nat Commun 2024;15:6069.
93. Wang Y, Douville C, Chien YW, Wang BG, Chen CL, Pinto A, et al. Aneuploidy landscape in precursors of ovarian cancer. Clin Cancer Res 2024;30:600–15.
94. Chien Y-W, Wang Y, Huang P, Lawson BC, Kolin DL, Chui MH, et al. Morphologic and molecular heterogeneity of high-grade serous carcinoma precursor lesions. Am J Surg Pathol 2024;48:475–86.
95. ICGC/TCGA Pan-Cancer Analysis of Whole Genomes Consortium. Pan-cancer analysis of whole genomes. Nature 2020;578:82–93.
96. Efe G, Rustgi AK, Prives C. p53 at the crossroads of tumor immunity. Nat Cancer 2024;5:983–95.
97. Berenblum I, Shubik P. An experimental study of the initiating state of carcinogenesis, and a re-examination of the somatic cell mutation theory of cancer. Br J Cancer 1949;3:109–18.

98. Balmain A. Peto's paradox revisited: black box vs mechanistic approaches to understanding the roles of mutations and promoting factors in cancer. Eur J Epidemiol 2023;38:1251–8.
99. Berenblum I, Shubik P. The persistence of latent tumour cells induced in the mouse's skin by a single application of 9:10-dimethyl-1:2-benzanthracene. Br J Cancer 1949;3:384–6.
100. Zhu M, Wang N, Wang S, Wang Y, Yang X, Fan J, et al. Effects of follicular fluid on physiological characteristics and differentiation of fallopian tube epithelial cells implicating for ovarian cancer pathogenesis. Int J Mol Sci 2023;24:10154.
101. Stangis M, Chen Z, Min J, Glass S, Jackson J, Radyk M, et al. The hallmarks of precancer. Cancer Discov 2024;14:683–9.
102. Haldar SD, Vilar E, Maitra A, Zaidi N. Worth a pound of cure? Emerging strategies and challenges in cancer immunoprevention. Cancer Prev Res (Phila) 2023;16:483–95.
103. Muhlich JL, Chen Y-A, Yapp C, Russell D, Santagata S, Sorger PK. Stitching and registering highly multiplexed whole-slide images of tissues and tumors using ASHLAR. Bioinformatics 2022;38:4613–21.
104. Yapp C, Novikov E, Jang W-D, Vallius T, Chen Y-A, Cicconet M, et al. UnMICST: deep learning with real augmentation for robust segmentation of highly multiplexed images of human tissues. Commun Biol 2022;5:1263.
105. Brooks M, Kristensen K, Benthem Kv, Magnusson A, Berg C, Nielsen A, et al. glmmTMB balances speed and flexibility among packages for zero-inflated generalized linear mixed modeling. R Journal 2017;9:378–400.
106. Harrison XA. Using observation-level random effects to model overdispersion in count data in ecology and evolution. PeerJ 2014;2:e616.
107. Schapiro D, Jackson HW, Raghuraman S, Fischer JR, Zanotelli VRT, Schulz D, et al. histoCAT: analysis of cell phenotypes and interactions in multiplex image cytometry data. Nat Methods 2017;14:873–6.
108. Rublee E, Rabaud V, Konolige K, Bradski G. ORB: an efficient alternative to SIFT or SURF. In: 2011 International Conference on Computer Vision [Internet]. 2011 [cited 2024 Aug 19]. p. 2564–71. Available from: https://ieeexplore.ieee.org/document/6126544.
109. Sammut S-J, Crispin-Ortuzar M, Chin S-F, Provenzano E, Bardwell HA, Ma W, et al. Multi-omic machine learning predictor of breast cancer therapy response. Nature 2022;601:623–9.
110. Bürkner PC. brms: an R package for Bayesian multilevel models using stan. J Stat Softw 2017;80:1–28.
111. Kruschke JK, Liddell TM. The Bayesian New Statistics: hypothesis testing, estimation, meta-analysis, and power analysis from a Bayesian perspective. Psychon Bull Rev 2018;25:178–206.